Dynamically Downscaled High-Resolution Hydroclimate Projections for Western Canada

ANDRE R. ERLER, W. RICHARD PELTIER, AND MARC D'ORGEVILLE

Department of Physics, University of Toronto, Toronto, Ontario, Canada

(Manuscript received 3 March 2014, in final form 14 August 2014)

ABSTRACT

Accurate identification of the impact of global warming on water resources in major river systems represents a significant challenge to the understanding of climate change on the regional scale. Here, dynamically downscaled climate projections for western Canada are presented, and impacts on hydrological variables in two major river basins, the Fraser and Athabasca, are discussed. These regions are both challenging because of the complexity of the topography and important because of the economic activity occurring within them. To obtain robust projections of future conditions, and to adequately characterize the impact of natural variability, a small initial condition ensemble of independently downscaled climate projections is employed. The Community Earth System Model, version 1 (CESM1), is used to generate the ensemble, which consists of four members. Downscaling is performed using the Weather Research and Forecasting Model, version 3.4.1 (WRF V3.4.1), in a nested configuration with two domains at 30- and 10-km resolution, respectively. The entire ensemble was integrated for a historical validation period and for a mid-twenty-first-century projection period [assuming representative concentration pathway 8.5 (RCP8.5) for the future trajectory of greenhouse gases]. The projections herein are characterized by an increase in winter precipitation for the mid-twenty-first-century period, whereas net precipitation in summer is projected to decrease, due to increased evapotranspiration. In the Fraser River basin, a shift to more liquid precipitation and earlier snowmelt will likely reduce the seasonal variability of runoff, in particular the spring freshet. In the Athabasca River basin, winter precipitation and snowmelt may increase somewhat, but increasing evapotranspiration may lead to reduced streamflow in late summer.

1. Introduction

Global climate models have become a well-established tool on the basis of which the impact of increased greenhouse gas concentrations and other forcings on the climate system may be assessed, but the majority of such models are currently able to deliver useful information only on large spatial and temporal scales. However, climate on regional scales, which is most relevant from the perspective of environmental policy, is strongly modified by land–water contrasts, steep topographic gradients, and land cover changes on scales that are only poorly resolved in global models, if they are resolved at all. In addition synoptic and mesoscale weather systems may interact with these unresolved features in complex, nonlinear ways, further undermining the utility of global model projections for local applications.

Western Canada, which for the purpose of this study will be taken to include the Canadian provinces of British Columbia and Alberta, is a region of extreme topographic gradients and land–sea contrasts, which also includes several large inland lakes, all of which may strongly affect local climate. The climate of British Columbia, west of the Continental Divide, is dominated by extremely high rates of orographic precipitation, especially in winter and closer to the coast. The Coast Mountains in this region are in fact among the regions of the world that receive the highest annual precipitation amounts, on par with most of the tropics (Mote and Salathé 2010; Schneider et al. 2014). Consequently British Columbia is largely covered by boreal rain forest and possesses significant hydrological resources. The plains and forested lowlands of Alberta to the east of the Continental Divide, on the other hand, lie in the rain shadow of the Rocky Mountains and

Corresponding author address: Andre R. Erler, Department of Physics, University of Toronto, 60 St. George St., Toronto ON M5S 1A7, Canada.
E-mail: aerler@atmosp.physics.utoronto.ca

DOI: 10.1175/JCLI-D-14-00174.1

receive relatively little precipitation (Burn 2008; Harris et al. 2014).

Hydroclimatic projections that resolve these regional differences, ideally on the scale of individual river basins, or smaller, are highly relevant for water resource analyses that are directed toward climate change impact mitigation and adaptation. To bridge the gap between the resolution of global climate models (GCMs) and the regional scales of interest, there has been a widespread and continuing effort to develop the numerical methodology required to downscale climate projections from global to regional scales (Giorgi 2006; Maraun et al. 2010). A relatively inexpensive methodology whereby this may be achieved is statistical downscaling, in which local climate variables are related to large-scale fields derived from GCM output. This method can also serve as a means of bias correction, but it cannot account for nonlinear effects and feedbacks in the climate system, such as those related to snow albedo or complex land–atmosphere interactions, or changes in the distribution of extreme events (Salathé et al. 2010; Gutmann et al. 2012).

A physically and dynamically more consistent but computationally much more expensive approach is dynamical downscaling, in which a limited area model is forced with output from a GCM at the lateral boundaries (and most often also with SSTs and sea ice from the driving GCM). Such limited area models are usually numerical weather prediction models that have been adapted for long-term simulations and are often referred to as regional climate models (RCMs), which are typically run at spatial resolutions in the range 20–50 km.

The goal of the present study is to develop and apply a state-of-the-art dynamical downscaling ''pipeline'' to obtain high spatial resolution projections of the global warming process for western Canada that directly address the expected impacts on the water resources represented by the two major river systems mentioned previously. Our primary goal is to provide detailed assessment, not only of the expected warming of the lower atmosphere in this region, but also of the change in the accompanying precipitation regime (both liquid and solid), which ultimately controls the target hydrographs. In these analyses we will be employing the Weather Research and Forecasting Model (WRF) as the regional model in a two-stage nested configuration in which the highest-resolution inner domain has a spatial resolution of 10 km. This regional model will be forced by global scale data from the Community Earth System Model, version 1 (CESM1), run at full resolution from phase 5 of the Coupled Model Intercomparison Project (CMIP5).

A recent study of particularly relevance to the work presented here is that of Salathé et al. (2010), who downscaled two global climate projections [one from the Community Climate System Model, version 3 (CCSM3), and one from ECHAM5], also using the WRF at 20- and 30-km resolution, respectively. Their area of interest was the U.S. state of Washington, which shares many characteristics with western Canada, including the existence of strong topographic gradients. Salathé et al. (2010) find a dramatic decrease in snowpack because of changes in precipitation, which are enhanced by higher spring temperatures due to the action of snow–albedo feedback. They furthermore show that changes in precipitation patterns are strongly modulated by topography, in a way that would not have been anticipated from thermodynamic arguments or changes in large-scale circulation patterns alone.

More recently, there have been clear demonstrations of the significant improvements to be realized simply by further increasing the spatial resolution over the target domain. For example, Gula and Peltier (2012) performed regional simulations at 10-km resolution over the Great Lakes region that lie along the eastern U.S.–Canada border, also using the WRF–CCSM3 combination. They show that at this level of resolution the winter snow belts that develop in the lee of each of the Great Lakes are well resolved (features that are entirely missing in the global model). Pollock and Bush (2013) performed simulations at 6-km resolution over parts of the Canadian Rocky Mountains, using the older Fifth-Generation Pennsylvania State University–National Center for Atmospheric Research (NCAR) Mesoscale Model (MM5), driven by a Geophysical Fluid Dynamics Laboratory (GFDL) GCM. They found that the spatial distribution of orographic precipitation patterns is very well simulated, but the intensity is significantly overestimated (by a factor of 2). Pollock and Bush (2013) attribute the excess precipitation to an underestimation of the rain shadow effect of the coastal mountain ranges due to insufficient resolution in the inflow region to their high-resolution domain (which did not include these mountain ranges). Rasmussen et al. (2011) have recently performed simulations at 2-km resolution for several model years over the Colorado Rockies again, using WRF, and report very good representations of the spatial distribution and intensity of precipitation, even though their high-resolution domain does not include upwind mountain ranges. However, in contrast to the other studies, they employed boundary conditions based only on the North American Regional Reanalysis (NARR) product, which, by design, accounts for major rain shadow effects (Mesinger et al. 2006). In summary, these studies have demonstrated that increased resolution significantly improves the representation of local climatic features, especially (and perhaps surprisingly) precipitation. In recognition of these developments, the

Coordinated Regional Downscaling Experiment (CORDEX; Giorgi et al. 2009) is now also encouraging the use of higher resolutions, close to 10 km or finer (Arritt and Rummukainen 2011).

While it is relatively simple to perform regional climate simulations with reanalysis data as boundary forcing, downscaling climate projections is more challenging because of the lack of a well-established offline coupling protocol between GCMs and RCMs. One product of the work described herein has been the development of an efficient and fully scripted pipeline, connecting the preprocessing system of the regional model with the output of the driving model. Furthermore, a common challenge in climate modeling is the validation process and the assessment of uncertainty. Because GCMs do not track the historical evolution of weather, each model integration provides an entirely independent realization of weather and climate. It is thus meaningless to compare model output directly with observations at scales that are dominated by natural variability. Only the long-term average and the statistical distribution of weather events can be meaningfully compared, which requires long integration periods and/or multiple realizations (Hawkins and Sutton 2009; Deser et al. 2012a). A corollary to the validation problem is that projections can only be understood in a probabilistic sense, and the range of possibilities (and uncertainties) has to be clearly communicated in order that the results may be meaningfully employed for policy development or other purposes. This problem extends to regional climate models that are driven by GCM output. In fact, it is further exacerbated because the uncertainty associated with natural variability on regional scales is as large as model uncertainty, and for mid-twenty-first-century projections it is larger than scenario uncertainty (e.g., Hawkins and Sutton 2009).

It is well known that different combinations of RCMs and GCMs can produce very different results (Giorgi 2006); also, for example, Salathé et al. (2010) report significant differences in some aspects of their two downscaled simulations. Furthermore Deser et al. (2012a) have demonstrated that even between realizations of a single global model, the differences in the precipitation field can be very significant, and many realizations are needed to achieve statistical significance. Traditionally this has been achieved by performing longer simulations; however, in transient simulations the ''background climate'' changes, so that depending on the length of the time slice multiple realizations have to be performed. In this study we use a small suite of dynamically downscaled climate projections, based on an initial condition ensemble of four independent global projections from the same GCM. This is in contrast to most previous studies that have relied on multimodel ensembles, if an ensemble was employed at all.

We will focus our hydroclimate analysis on two important river basins, namely the Fraser River basin in British Columbia and the Athabasca River basin in Alberta. Both have their headwaters in the Rocky Mountains; the Fraser flows to the west and drains into the Pacific Ocean near the city of Vancouver, whereas the Athabasca runs east into the lowlands of Alberta, and drains into Lake Athabasca (cf. Fig. 1). The latter region is of special interest, as it is host to the bitumen extraction industry (the so-called oil sands), which relies heavily upon water resources provided by the Athabasca River. Ultimately, an assessment of the impact of global warming on water resources will require detailed surface and subsurface hydrological modeling, which is beyond the scope of the present study. Nevertheless, an analysis of hydroclimatic variables over a single drainage basin can provide valuable insights into likely changes to runoff and streamflow. The response of annual and seasonal streamflow to idealized warming in different seasons in the western United States was studied by Das et al. (2011), using a hydrological model in pseudo–global warming experiments, where artificial warming was applied for specific months and seasons separately. Their results suggest that warming during the warm season uniformly reduces annual and summer streamflow due to increased evapotranspiration, whereas cold season warming increases streamflow in the cold season due to early snowmelt, but reduces streamflow in the warm season. The results of Das et al. (2011) for the Columbia and Colorado Rivers can serve as analogs for our interpretation of hydroclimatic changes in the Fraser and Athabasca River basins, respectively. Also immediately relevant in this context are the hydrological analyses of Shrestha et al. (2012) and Kerkhoven and Gan (2011), both of whom employed bias-corrected input derived from phase 3 of the Coupled Model Intercomparison Project (CMIP3) GCM projections to drive a hydrological model. While Shrestha et al. (2012) only considered the Fraser River basin and its subbasins, Kerkhoven and Gan (2011) produced hydrological projections for both of the two river basins upon which we focus in the present paper, using much higher-resolution dynamically downscaled climate projections. For the Fraser River, both studies report a decrease in peak flow, but only small changes in the annual discharge. For the Athabasca River, Kerkhoven and Gan (2011) find a clear reduction in late summer streamflow in all of their simulations, but some also show an increase in the peak seasonal flow. These two analyses will provide a further point of comparison for our own analysis.

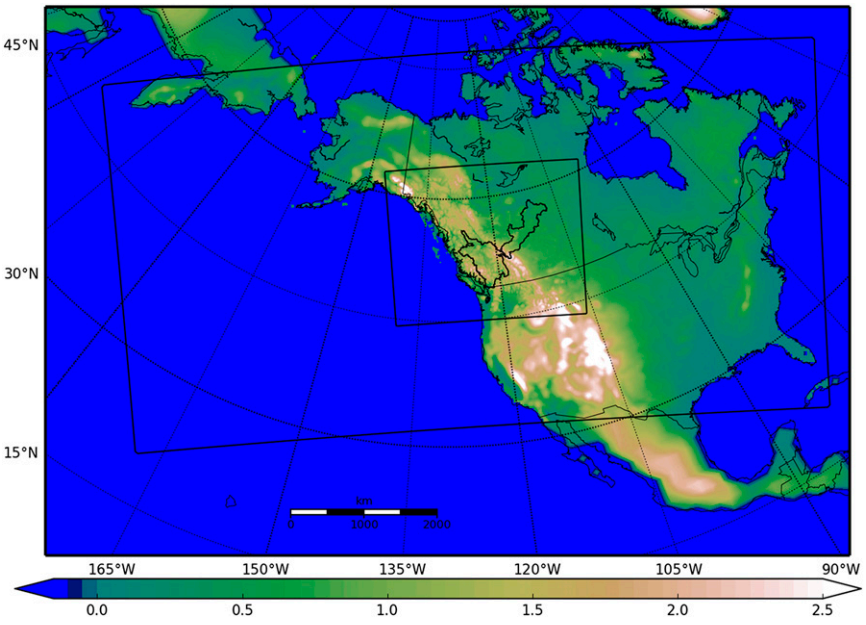

FIG. 1. Topography and outline of the outer and inner WRF domains as well as the outlines of the Fraser (left) and Athabasca (right) River basins shown inside the inner domain. Note that the coastline indicated on the map represents the actual coastline at a resolution comparable to the inner WRF domain; it does not necessarily match the coastlines in the models.

This article is structured as follows: first the experimental design and model configurations are introduced. The validation of the modeling chain is discussed next, before climate projections for the mid-twenty-first century are presented. This is followed by an analysis of the hydroclimate of the Fraser and Athabasca River basins, before we close with a discussion of the impact and the large-scale drivers of natural variability.

The following definitions of seasons are used throughout this article: spring is March–May (MAM), summer is June–August (JJA), fall is September–November (SON), and winter is December–February (DJF).

2. Climate models and experimental design

To provide hydroclimatic projections on a regional and river basin scale, a regional climate model has been employed to dynamically downscale a set of four global climate projections for western Canada. The global projections were generated using the NCAR Community Earth System Model [CESM (version 1.04), see below for details]. Four independent model integrations were preformed, using an identical model configuration but different initial conditions in the preindustrial era, so as to produce a small initial condition ensemble on the basis of which internal variability can be characterized. The initial conditions were obtained from a preindustrial equilibrium integration and were spaced 15 years apart; the transient forcing begins with conditions corresponding to the year 1850 CE. The regional model used for downscaling is the NCAR Weather Research and Forecasting Model, version 3.4.1 (WRF V3.4.1, see below for details), run in a nested configuration with an outer domain at 30-km resolution and an inner domain at 10-km resolution. The outer domain covers most of North America and the northeastern Pacific, while the inner domain basically covers only the Canadian Provinces of Alberta and British Columbia (east and west of the Rocky Mountains, respectively). The representation of the topography and outlines of the outer and inner domains as well as the Fraser and the Athabasca River basins are shown in Fig. 1.

The global model was run continuously from the preindustrial era (starting in 1870), but only two 15-yr segments were downscaled with the regional model because of the much higher computational cost of the regional model. The historical validation period ranges from 1979 to 1994 and the future projection period from 2045 to 2060. Only one scenario, representative concentration pathway 8.5 (RCP8.5), was considered, because the concentrations do not diverge significantly until the second half of the twenty-first century except for the stabilization pathway, which is arguably very unlikely to be realized. RCP8.5 corresponds to a CO_2 concentration of 540 ppmv in 2050, which is slightly above the older Special Report on Emissions Scenarios

A1B and A2 scenarios and most closely resembles the current trajectory. For a discussion of how CESM responds to different forcing scenarios (including RCP8.5) on a global scale, see Meehl et al. (2012).

a. CESM configuration

The Community Earth System Model (Gent et al. 2011) is a fully coupled global climate model developed by the National Center for Atmospheric Research. CESM has a modular structure with submodules for all major Earth system components; in this work all major components of the physical climate system (atmosphere, ocean, sea ice, and land surface) have been employed. The atmospheric component is the Community Atmosphere Model, version 4 (CAM4; Neale et al. 2013), which operates with a finite volume hydrostatic dynamical core on a regular geographic (latitude–longitude) grid with terrain-following hybrid-pressure coordinates. The resolution of the atmosphere model is approximately 1.25° × 0.9° in the horizontal, with 26 vertical layers (spaced more closely at the surface). The ocean model used in CESM is the Parallel Ocean Program (POP) version 2 (Danabasoglu et al. 2012). It also employs a finite-volume dynamical core with explicit time stepping. The grid has 60 levels (with higher resolution near the surface) and a nominal zonal resolution of about 1°; the meridional grid spacing is 0.27° at the equator, increasing to 0.54° at high latitudes. The coordinate system is spherical–polar, but the Northern Hemisphere is distorted, such that the coordinate pole lies over Greenland. The land surface model used in CESM is the Community Land Model, version 4 (CLM4; Lawrence et al. 2012); it runs on the same grid and with the same time step as the atmospheric model. The land model handles all surface processes, such as soil and canopy evapotranspiration and surface heat fluxes. It predicts soil moisture and temperature on 15 layers and features a five-layer snow model. CLM also includes a dynamic vegetation model, but this option was not used in the simulations presented here; the predictive carbon and nitrogen cycle module was employed, however. Runoff is handled through a river-routing scheme, but the soil does not interact with aquifers or deep groundwater. Sea ice in CESM is simulated using the Los Alamos sea ice model, the Community Ice Code version 4 (CICE; Holland et al. 2012). CICE is an elastic–anisotropic–plastic sea ice model and runs on the same grid as the ocean model. It has subgrid-scale ice thickness and snow classes and a state-of-the-art radiation module that includes an advanced albedo calculation and a melt-pond parameterization. Sea ice plays an important role in mediating fluxes between the ocean and the atmosphere, and in this version of the model sea ice also exhibits significant internal variability on decadal time scales (Jahn et al. 2012).

b. WRF configuration

WRF is a state-of-the-art nonhydrostatic limited-area weather forecast and research model (Skamarock and Klemp 2008) that is increasingly being used for long-term climate simulations (Fita et al. 2009). For the simulations presented here, version 3.4.1 was employed, but the following two additional modifications were implemented: 1) a simple lake model (FLake) was added to WRF, as described in Gula and Peltier (2012), but now coupled online, and 2) the Rapid Radiative Transfer Model for GCMs (RRTMG) radiation scheme was modified to support variable greenhouse gas concentrations as prescribed by the RCP scenarios. All WRF simulations presented here were obtained with the same model configuration, using the following physical parameterization schemes: the RRTMG radiation scheme for shortwave and longwave radiation (Iacono et al. 2008), the Morrison two-moment microphysics scheme (Morrison et al. 2009), the Grell 3D ensemble cumulus scheme (with shallow cumulus and subsidence spreading enabled; Grell and Dévényi 2002), the Mellor–Yamada–Nakanishi–Niino level 2.5 boundary and surface layer options (Nakanishi and Niino 2009), and the unified Noah land surface model (Noah LSM, with urban canopy model; Tewari et al. 2004). Numerous sensitivity tests have been performed and validated against observational data, and the configuration described above was found to yield the best agreement with observations. In particular, compared to the regional climate configuration recommended in the WRF user guide (Wang et al. 2012), the RRTMG radiation scheme significantly improved simulated surface temperatures, the Grell 3D cumulus scheme significantly improved summer precipitation patterns, and the use of a two-moment microphysics scheme improved winter temperatures and precipitation. Cassano et al. (2011) also found similar improvements from using the RRTMG radiation scheme over their Arctic domain; however, they also report deteriorating performance with the Morrison two-moment microphysics scheme, which we cannot confirm. Rasmussen et al. (2011) find significant improvements in orographic precipitation with the Thompson and the Morrison two-moment scheme over the Colorado Rockies, consistent with our results.

For the internal representation of the coordinate system in WRF a Lambert conformal conic projection was chosen, which minimizes distortion for midlatitudes and preserves angles. The projection (and outer domain) is centered at 55°N, 125°W, with the latitudes of true scale at 43°N and 61°N. The outer domain (at 30-km

resolution) has 320 × 170 grid points, and the inner domain (at 10-km resolution) has 262 × 211 grid points [the lower left corner of the inner domain is located at grid point (124, 49) in the outer domain]; the time steps are 150 and 50 s, respectively. In both domains 28 vertical levels were employed with closer spacing in the boundary layer and the model top at 50 hPa. Because of the large topographic gradients in the Rocky Mountains it was also necessary to enable the vertical velocity damping option and to choose a larger time off-centering coefficient of $\beta = 0.5$ in the vertical acoustic time-stepping scheme[1] in order to maintain stability. Despite these measures, numerical instabilities occurred frequently, and on many occasions the time step had to be temporarily reduced to as little as 20 s in the inner domain.

The lateral boundary conditions from CESM were prescribed to WRF at the outermost grid point, and the WRF solution was nudged toward the lateral boundary conditions over the adjacent nine grid points. Sea surface temperatures and fractional sea ice were also prescribed from CESM at the lower boundary, but no land surface parameters from CESM were supplied to WRF (standard tabulated values were employed). To prevent boundary-induced waveguide effects and drift of the large-scale fields in the interior of the domain spectral nudging (Miguez-Macho et al. 2004) toward the CESM solution was applied to the outer domain above the boundary layer at scales larger than about 3000 km. All CESM forcing data were processed offline and supplied to WRF at regular 6-hourly intervals.

c. *Observational datasets employed for validation*

Validation against observational data is critical for any numerical modeling endeavor. Thus, the downscaled climate simulations have been validated against several gridded observational datasets: the University of East Anglia Climatic Research Unit (CRU) 0.5° multivariate monthly time series (Harris et al. 2014) and the Global Precipitation Climatology Centre (GPCC) 0.5° monthly precipitation time series and 0.25° climatology (Schneider et al. 2014). The CRU and GPCC time series are available from 1901 to 2012, while the higher-resolution GPCC climatology is based on the period from 1951 to 2001. The cornerstone of our validation, however, is formed by the very high-resolution ($^1/_{48}° \approx 3.3$ km) Parameter-Elevation Regressions on Independent Slopes Model (PRISM) temperature and precipitation climatology, based on the period from 1979 to 2009. It should be noted that PRISM contains an altitude- and slope-based correction for orographic effects, and is thus not purely observational (Daly et al. 2008). However, since the distribution of weather stations is significantly biased, with more stations in valleys and flatlands than on mountain tops and slopes, orographically corrected datasets and recently also high-resolution numerical models (cf. Rasmussen et al. 2011) arguably provide a better estimate of precipitation in mountainous terrain than simply interpolated observations.

At the time of writing, PRISM data for Canada are only available west of 113°W, which does not include parts of the Athabasca River basin, and for that reason, and in order to streamline the validation process, we have assembled a merged validation dataset that consists of PRISM data where available (temperature and precipitation west of 113°W) and otherwise CRU temperature data (at 0.5°, averaged from 1979 to 2009) and GPCC precipitation data (at 0.25° resolution). Because the GPCC climatology and the PRISM climatology have different reference periods, we have subtracted the (interpolated) 0.5° GPCC climatology from the 0.25° climatology (which are based on the same period), and then added the (interpolated) time average of the 0.5° GPCC time series from 1979 to 2009 back into the 0.25° climatology. The entire dataset was then adjusted once more in a similar way for the time period from 1979 to 1994, using monthly anomalies from the 0.5° CRU and GPCC time series (for temperature and precipitation, respectively). Gutmann et al. (2012) argue for the use of long-term climatologies for precipitation validation, rather than only averaging over the period that was simulated. The purpose of this is to increase the statistical significance of sparse observations and reduce noise. We find this to be unnecessary in our case, because the high-resolution component of the precipitation and temperature fields was in fact derived from a 30-yr climatology (PRISM), and the validation period of 15 years is long enough to remove noise in the low-resolution anomaly fields (CRU and GPCC at 0.5°). The differences in the merged precipitation climatology averaged over 15, 30, or even 60 yr are in fact imperceptible; differences between 15- and 10-yr averages are small, but visible in the seasonal cycle (averaged over a basin, 5%–10% in some months).

If not otherwise noted, all datasets have been reprojected and resampled onto the 10-km grid of the inner WRF domain before assembling the merged dataset. The resulting annual mean precipitation from this merged observational dataset is shown in Fig. 2 (top right). Further note that gridded (in situ) observational datasets are only available over land; no data are

[1] That means the numerical operator was biased toward the implicit component of the solution (cf. Skamarock et al. 2008), which improves stability, but reduces the numerical accuracy.

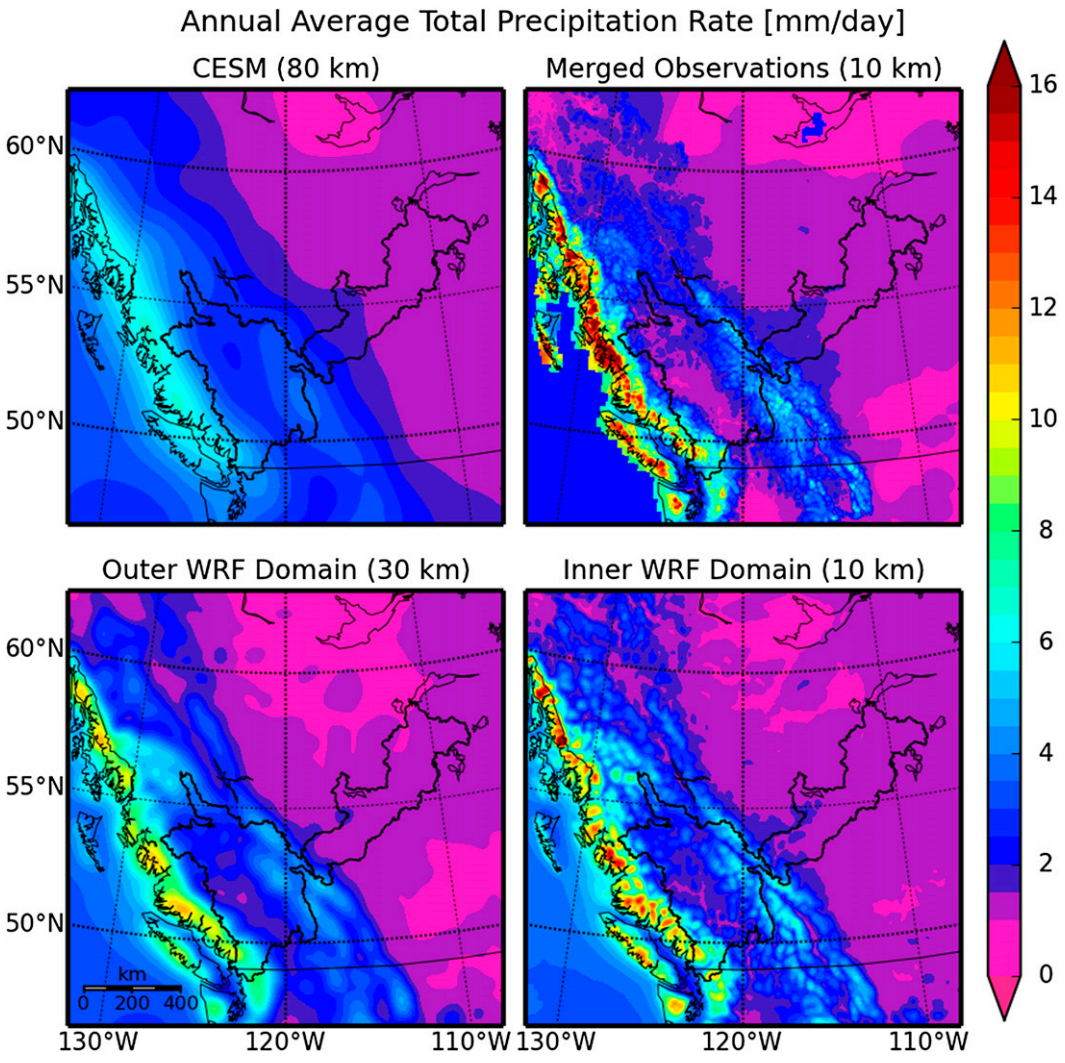

FIG. 2. Annual total precipitation averaged over 15 yr (1979–94): (top right) the merged observational dataset and (top left) the ensemble means of CESM (~80 km), (bottom left) the outer WRF domain (30 km), and (bottom right) the inner WRF domain (10 km). The outlines of the Fraser and Athabasca River basins are also shown.

available over large water bodies, and no validation was therefore performed.

RIVER DISCHARGE DATA

In section 4 runoff from the Noah LSM will be compared to observed river discharge from gauge stations close to the point where the main river exits the basin. The data were obtained from the Water Survey of Canada (Environment Canada; publicly available at http://www.wsc.ec.gc.ca/applications/H2O/index-eng.cfm).

The station employed for the Fraser River basin is Port Mann pumping station (08MH126), located at 49°13′4″N, 122°49′37″W, which has a record of 18 yr (1965–72 and 1983–92, inclusive). For the Athabasca River basin the station at Embarras Airport (07DD001), located at 58°12′18″N, 111°23′24″W, was employed, which has a record of 14-yr duration (1971–84, inclusive). Not all years in the station record have complete monthly data; nevertheless, all available flow data have been used in the averaged monthly discharge climatologies in section 4. The records we have employed here were last revised in 2010.

d. Indices of climate variability

In section 5b indices of large-scale climate variability will be discussed. These indices have been computed using the Climate Variability Diagnostics Package (CVDP, version 3.2.0; Phillips et al. 2014, and references therein) from NCAR's Climate Analysis Section. The datasets that were used to obtain the indices for the historical period (also referred to as ''observations'') are the Hadley Centre Sea Ice and Sea Surface Temperature

dataset [HadISST; Rayner et al. 2003; for Niño-3.4, the Atlantic multidecadal oscillation (AMO), and the Pacific decadal oscillation (PDO)] and the 20th Century Reanalysis for sea level pressure [version 2; Compo et al. 2011; for the North Pacific Oscillation (NPO), North Pacific index (NPI), North Atlantic Oscillation (NAO), northern annual mode (NAM), and Pacific–North American pattern (PNA)].

For the observations the indices and their associated empirical orthogonal functions (EOFs) were computed from the historical record from 1920 to 2011 for both datasets. To compute the same quantities for the CESM ensemble members, all time series from each member for a given period (validation or projection) were concatenated and for the purpose of computation treated as a single continuous simulation. The indices were only computed for CESM, not for WRF.

The time series were separated again so that they can be associated with individual ensemble members. However, correlation coefficients between climate indices and basin-averaged climatological variables were again computed from concatenated time series (the climatological variables were concatenated in the same way). Prior to computation, the mean was removed from the time series and it was divided by the standard deviation. Furthermore, the time series have also been smoothed with an 11-yr Hanning window and this might introduce spurious noise in the concatenated time series. However, the correlations are about 20% weaker in the unfiltered time series, albeit qualitatively similar. The time series have not been detrended, since the ensemble only runs over a short time period.

3. Validation and future projections

The purpose of this endeavor is, ultimately, to produce useful projections of future climate. To be useful, projections need to be credible, and uncertainties have to be accurately characterized. To establish confidence in the projections presented here, it is first necessary to validate the entire modeling pipeline against historical observations. Because of the increased availability of data, the period of 1979–94 is used as the validation period, while the target period for projection is 2045–60. The projection period is far enough in the future that significant climate change can already be expected, but is still close enough to the present to be policy relevant.

a. Validation against historical observations

Figure 2 shows annually averaged precipitation climatologies for CESM (top left) and the inner and outer WRF domains (bottom), along with the merged observational climatology (top right). The general pattern of precipitation in observations is one of very high precipitation intensities in the coastal mountains contrasted by very low annual precipitation rates in the rain shadows of the major mountain ranges, in particular in the inner plateau, which constitutes a major part of the Fraser River basin, and in the lee of the Rocky Mountains in the lowlands of Alberta (which comprises most of the Athabasca River basin). It is evident that the low-resolution global model significantly underestimates both the peak intensities in the Coast Mountains as well as the rain shadow effect in their lee. With increasing resolution the representation of orographic precipitation dramatically improves, although even the innermost WRF domain at 10-km resolution still underestimates the highest intensities seen in the observations and consequently produces too much precipitation over the regions located in the rain shadows.

Figure 3 shows the absolute temperature bias for the WRF ensemble mean (top) and the CESM ensemble mean (inner domain; bottom). Differences are shown for the annual mean (left) as well as the summer (center) and winter (right) seasonal averages. The differences were computed with respect to the merged observations (cf. section 2c), which have been reprojected and resampled to the native grid of each model. CESM has a cold bias in the Rocky Mountains and a warm bias in the lowlands in their lee, while WRF has an overall cold bias. The annual mean cold bias in WRF (−1.3°C) is primarily caused by a significant cold bias in spring (−3.4°C), while summer and winter temperatures are simulated fairly well (−0.5° and −0.1°C bias) by WRF, in particular in the lowlands. CESM has a significant warm bias in summer in large parts of the domain, which WRF does not have. In winter the pattern of biases is fairly similar, including a consistent cold bias at higher surface elevations in both CESM and WRF. All biases reported in this section refer to averages over the entire inner WRF domain, which is larger than the area shown in Figs. 2–8.

The absolute precipitation bias is shown in Fig. 4 (WRF, top and CESM, bottom). Again, differences are evident for the annual mean, summer, and winter (left, center, and right, respectively). Both models, CESM and WRF, show a similar pattern of biases in the seasonal cycle: winter precipitation is overestimated, except at the first rain barrier (where it is underestimated), whereas summer precipitation is generally underestimated. The main difference is that the seasonal biases are amplified in CESM and the fairly good match in annual precipitation rates is partly a consequence of opposite and compensating biases in summer and winter. The underestimation of precipitation at the first rain barrier and subsequent overestimation of precipitation in the rain shadow can also be seen in the regional simulations of Salathé et al. (2010) and Pollock and Bush (2013).

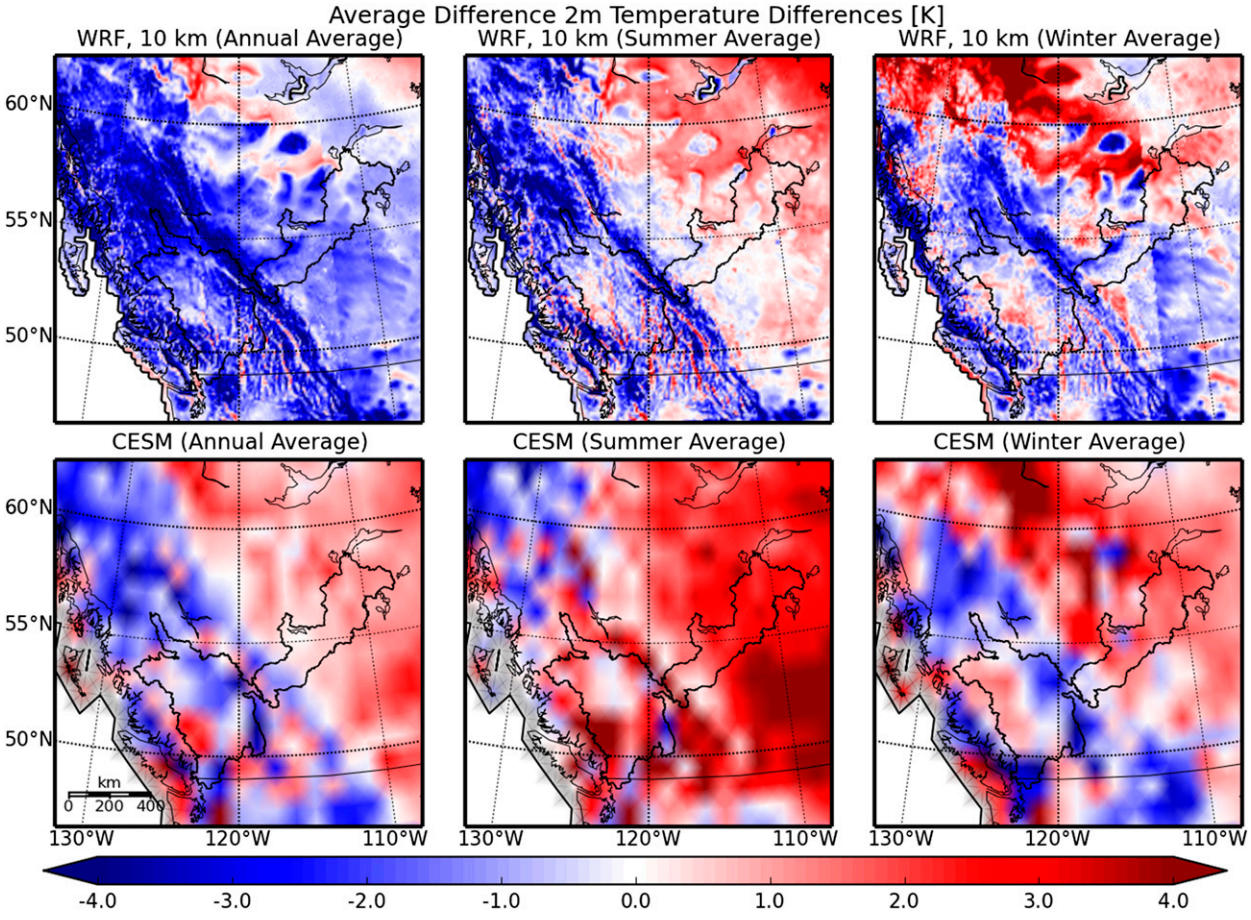

FIG. 3. (left) Annual mean, (center) summer, and (right) winter differences of 2-m air temperature with respect to the merged observational dataset, averaged over 15 yr: (top) inner WRF domain ensemble mean and (bottom) CESM ensemble mean.

It should be noted that most of the orographic precipitation, which dominates the spatial pattern, falls as grid-scale precipitation in winter, which means that it is directly affected by model resolution and microphysics, but not by the cumulus parameterization. Furthermore, the pattern of winter precipitation closely resembles the annual precipitation field (albeit with higher precipitation rates and enhanced orographic contrast). Summer precipitation, on the other hand, is predominantly convective and exhibits much higher spatial variability. Figure 5 shows the 15-yr average summer precipitation field for the four WRF ensemble members along with the observed summer precipitation and summer precipitation from the well-known NARR product (Mesinger et al. 2006), for comparison. In terms of the spatial pattern and intensity, WRF (at 10 km) clearly outperforms NARR, even though NARR assimilates precipitation data. The variability in the lowlands east of the Rocky Mountains is clearly much higher in WRF, and the observations lie at the higher end of precipitation amounts spanned by the WRF ensemble. In the ensemble mean, WRF underestimates summer precipitation compared to historical observations.

In passing we note that the North Pacific index and the PDO phase were significantly negative during the validation period whereas our ensemble is on average in a neutral phase; a negative NPI and PDO is associated with a drier winter and warmer spring (Trenberth and Hurrell 1994; Burn 2008, also see section 5b). This is consistent with precipitation and temperature data from the historical observations (CRU and GPCC), and there is also some indication that the validation period is wetter in summer relative to the preceding decades.

It is also interesting to note that temperature biases generally show less similarity between CESM and WRF than precipitation biases (if one accounts for the differences in resolution), and there is more similarity between CESM and WRF in the cold season than in the warm season. The differences in spring and summer temperatures between CESM and WRF are likely related to parameterized surface–atmosphere interactions, which act on a local scale, whereas the climate in winter is more

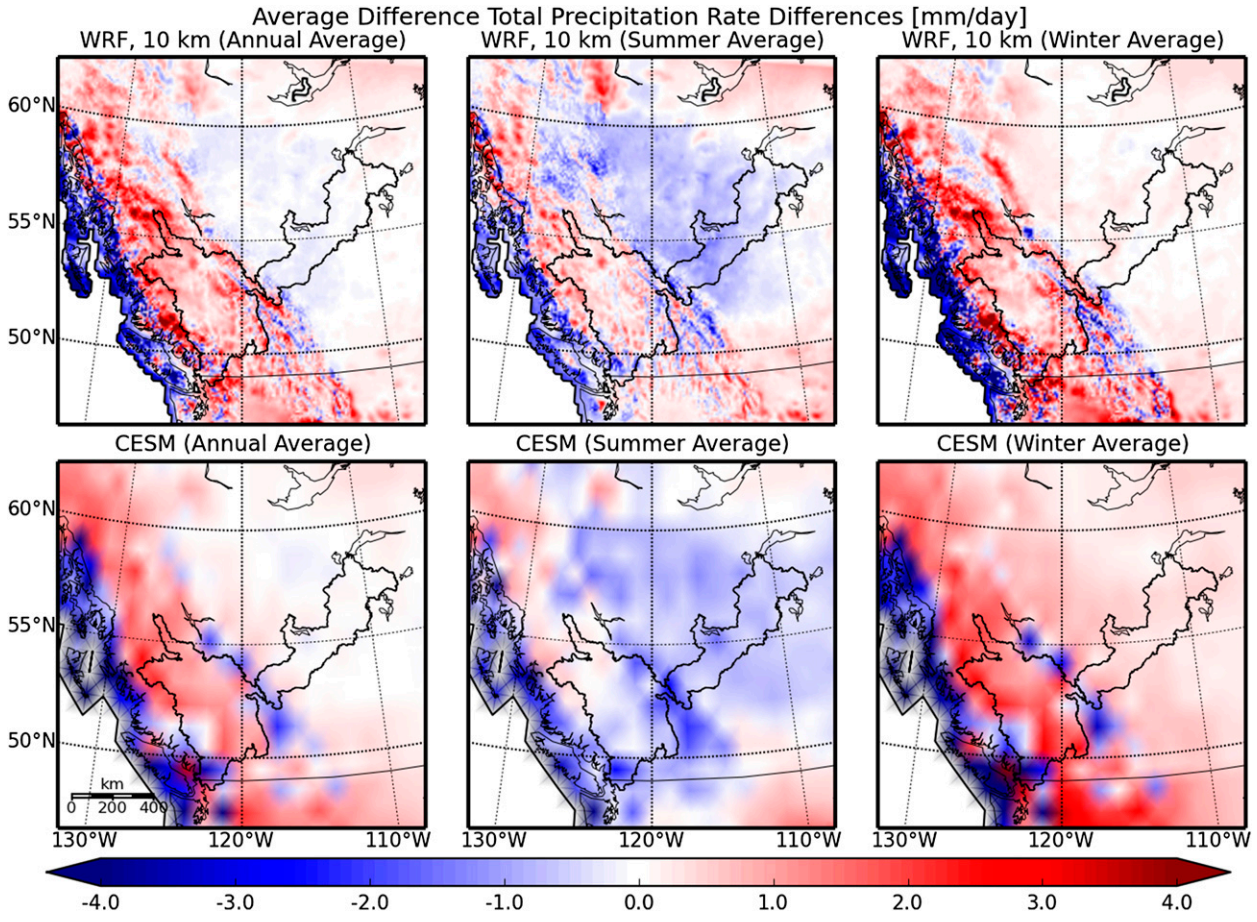

FIG. 4. (left) Annual mean, (center) summer, and (right) winter differences of total precipitation with respect to the merged observational dataset, averaged over 15 yr: (top) inner WRF domain ensemble mean and (bottom) CESM ensemble mean.

dominated by large-scale weather systems, which would be more consistent between WRF and CESM. The spring cold bias in WRF is probably caused by a poor representation of snowmelt processes combined with excess winter precipitation, which results in an impact of snow–albedo feedback on temperature. The higher summer temperatures in the arid lowlands in CESM are likely caused by a slower rate of precipitation recycling, which results in higher surface temperatures due to reduced latent heat flux at the surface (Seneviratne et al. 2010; see also section 3c).[2]

[2] When WRF is coupled to CLM4 (the land model used in CESM; Jin and Wen 2012) instead of the Noah LSM, we find that surface air temperatures closely follow those in CESM, including higher spring temperatures and higher temperatures in summer in the lee of the Rockies; apart from the resolution, the pattern of the temperature bias almost exactly matches that in CESM. Furthermore, with CLM4 (coupled to WRF or in CESM) the summer precipitation in the lowlands of Alberta is also reduced, owing to lower evapotranspiration and a lower rate of precipitation recycling.

b. *Mid-twenty-first-century projections*

Figure 6 shows the warming signal (average temperature differences between projection and validation periods) for the CESM and WRF (inner domain) ensemble means (same layout as Figs. 3 and 4). The annual mean signal is fairly consistent between WRF and CESM (2.4° and 2.6°C), and both models are characterized by strong polar amplification in winter (~2°C more than the domain average warming) and less warming in high latitudes in summer (~2°C below the domain average warming). But once more there are differences in the seasonal averages: in summer WRF has generally less warming (2.1° versus 2.6°C) but shows more warming at higher elevations (which are not resolved in CESM); in winter WRF actually predicts slightly more warming (2.6° versus 2.5°C) than CESM resulting from a slightly stronger polar amplification. Since the largest differences between WRF and CESM occur in summer, it is unlikely that they are caused by the relatively simple representation of snow in the Noah LSM. The large warming in the lowlands in CESM may

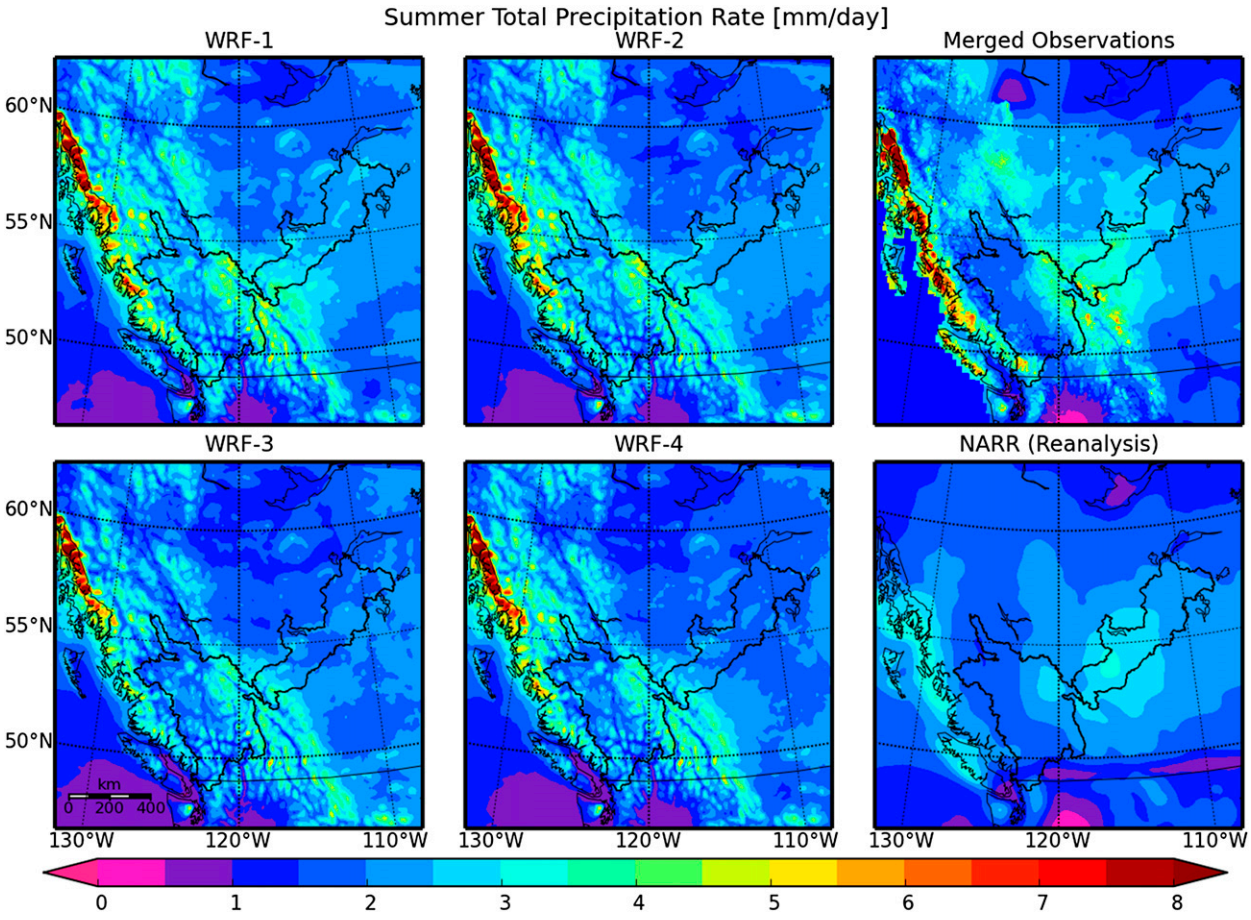

FIG. 5. Summer precipitation averaged over 15 yr for (left),(center) each of the WRF ensemble members (inner domain), (top right) the merged observation, and (bottom right) the NARR reanalysis product.

be due to the drier and warmer climate simulated by CESM in this region, which becomes even drier during the projection period (cf. Fig. 7). These climates are typically more sensitive to warming (Koster et al. 2004; Seneviratne et al. 2010) resulting from a smaller capacity for latent heat–related cooling at the surface. The differences along the Pacific coastal regions are almost certainly explained by interpolation errors in the sea surface temperature, because CESM does not resolve the complex coast line and islands, so that the affected grid points are part of the continent in CESM, but in WRF they are correctly treated as ocean grid points.

High-elevation areas are considered to be particularly sensitive to climate change, and enhanced warming would be expected in these areas in the Rocky Mountains. This effect is captured in the high-resolution WRF simulations but appears only in summer, whereas it is not captured in CESM. Pollock and Bush (2013) also find enhanced warming at high elevations in their simulations but also in the annual mean. They attribute this effect to enhanced diabatic heating, associated with increased orographic precipitation. However, the fact that in our simulations enhanced warming only occurs in summer, when orographic precipitation is relatively weak (and does not increase; see below), makes this explanation unlikely. Instead it is much more likely that the enhanced warming is caused by a snow–albedo feedback, because of earlier snowmelt (cf. Salathé et al. 2010). In winter, the snow cover at high elevations is continuous and robust, but the same effect is at play at lower elevations, where winter snow cover is not continuous and even modest warming can cause the thinner snow cover to recede, and initiate a positive feedback, causing even more warming. Winter warming is indeed enhanced in the lowlands.

The impact of global warming on precipitation patterns is less clear. Both CESM and WRF suggest that annual mean precipitation increases by 4% and 6%, respectively, with most of the increase in the shoulder seasons (5% and 6% in fall and 10% and 11% in spring, respectively). In CESM, however, the increase in winter is more modest than in WRF (3% versus 5%), and in

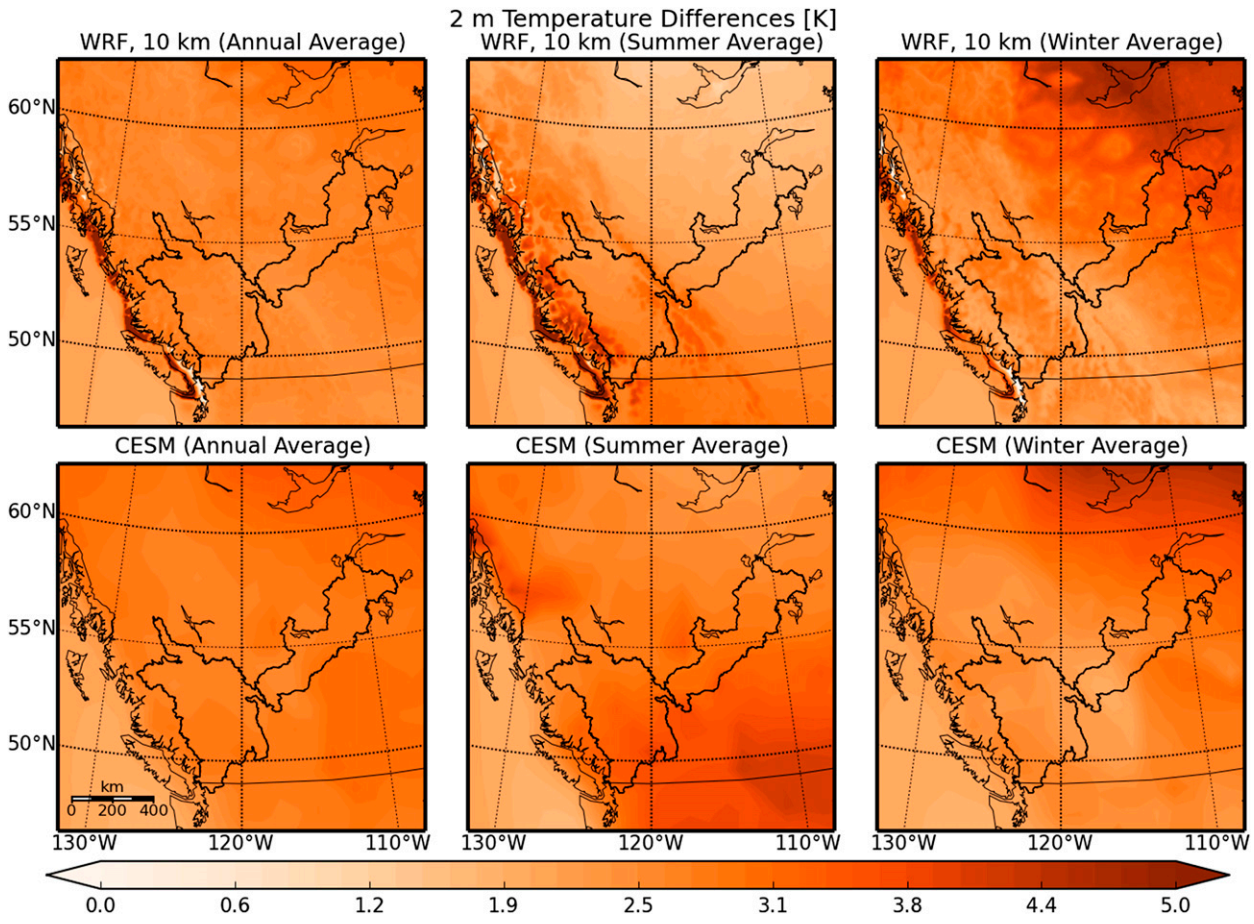

FIG. 6. Temperature changes between the mid-twenty-first-century projection period and the validation period; (left) annual mean, (center) summer, and (right) winter seasonal averages for (top) the inner WRF domain (ensemble mean) and (bottom) CESM (ensemble mean).

summer CESM actually predicts a small decrease (−3%) compared to a more uniform increase in WRF (5%). These are, however, ensemble means, and there is also a WRF ensemble member in which summer precipitation decreases significantly (see section 5a). Also note that these averages include the St. Elias Mountains and high-latitude regions, which are of less concern in the present study. Figure 7 shows the change of precipitation between the validation and the projection periods (same layout as in Fig. 6). It is evident that most of the increase occurs at higher latitudes.

During the summer season CESM simulates a decline in precipitation in large parts of the area of interest (the Fraser River basin and parts of the Athabasca River basin). WRF also simulates a decline in some areas but an increase in others. However, the meridional gradient of precipitation change is relatively consistent between WRF and CESM ensemble means, which suggests some degree of large-scale influence. However, the sign and regional pattern of the summer precipitation change is not consistent between ensemble members and the ensemble mean change in the area of interest is not significant in either direction. The precipitation increase in the cold season (fall and winter), appears to be fairly uniform (in terms of absolute differences), except for the front ranges of the Coast Mountains, where the increase in precipitation is significantly larger in WRF. However, these are also the areas with the highest climatological precipitation (and much higher precipitation in WRF), so that the relative increase is only approximately 10% in winter (which is well below the thermodynamic limit of 7% $°C^{-1}$; Trenberth et al. 2003). This apparent orographic enhancement appears considerably muted in the lower-resolution outer domain of WRF, and is not captured in CESM. Insufficient resolution can explain at least part of the discrepancy, but is unlikely to account for the opposite sign of the change predicted by CESM in some regions. Also note the increased rain shadow effect, especially over Vancouver Island, which suggests a change in tropospheric winds relative to the topographic gradient.

Compared to the results from the pseudoglobal warming experiment of Rasmussen et al. (2011), the increase in

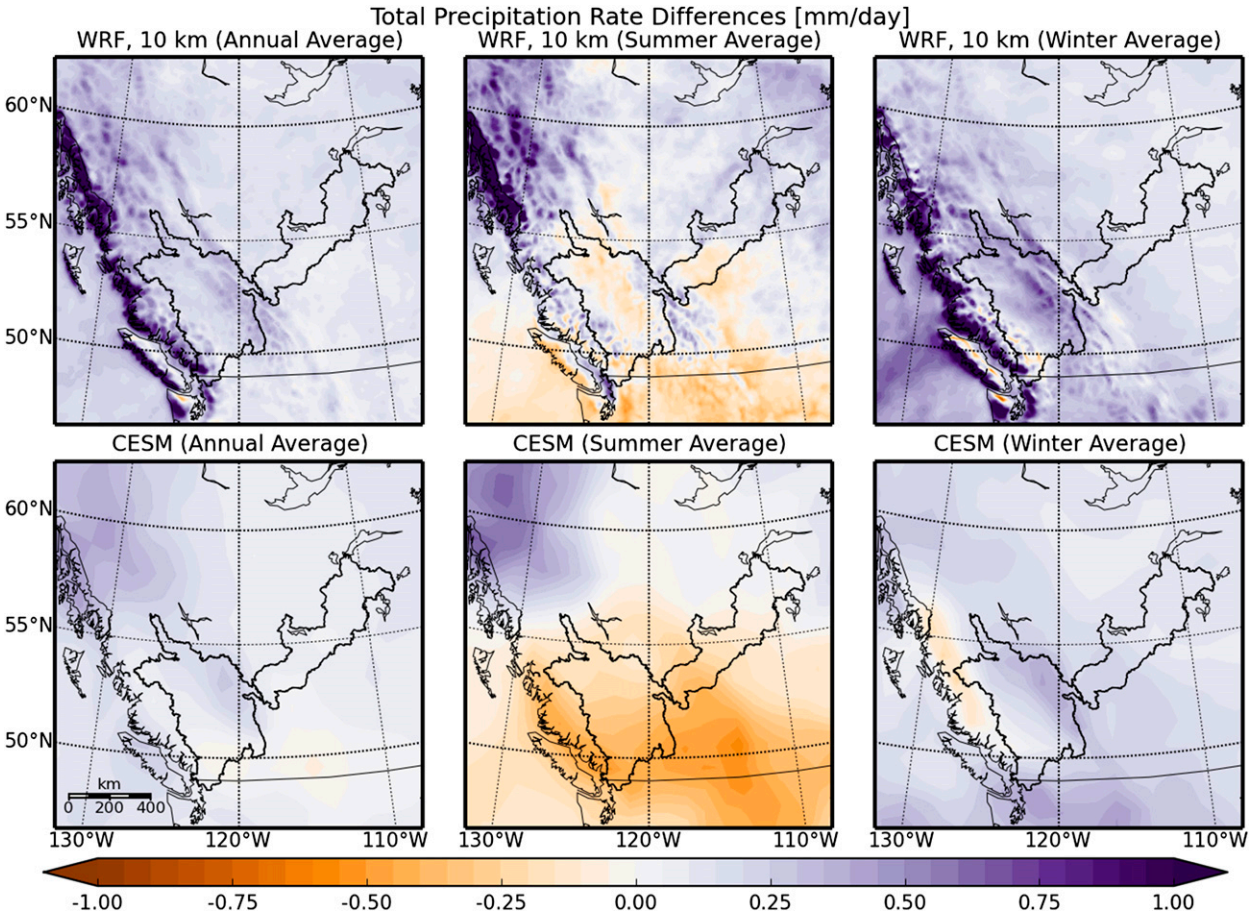

FIG. 7. Absolute precipitation changes between the validation and projection period; (left) annual mean, (center) summer, and (right) winter seasonal averages for (top) the inner WRF domain (ensemble mean) and (bottom) CESM (ensemble mean).

winter precipitation in our simulations [~10% versus 10%–25% in Rasmussen et al. (2011)] is at the lower end of their range. However, we find a very high degree of variability in the average precipitation changes in our ensemble, spanning an even larger range than that of Rasmussen et al. (2011). In fact the differences between WRF ensemble members (averaged over the inner domain) are of approximately the same magnitude as the predicted changes due to increases in greenhouse gas concentrations (in all seasons). For example, the changes in the winter season are +0.5%, +7%, +8%, and +23%, whereas the corresponding changes in the CESM ensemble are 0%, +1%, +5%, and +18%.

The more modest changes seen in our simulations are consistent with a trend recently identified by Luce et al. (2013). Based upon Snowpack Telemetry (SNOTEL) observations and streamflow data, they show that precipitation in the Pacific Northwest has been decreasing since the 1950s. They link this decrease to a slowing of lower tropospheric zonal winds in this region, which would reduce the orographic enhancement of precipitation. Using projections from CMIP5 GCMs, they furthermore show that this trend is expected to continue. The decrease resulting from reduced orographic enhancement, combined with the increase that might be expected from thermodynamic changes alone, could then result in a more modest increase, closer to what is seen in our simulations.

Salathé et al. (2010) also report significantly different and even divergent changes in orographic precipitation between the global models and their regional simulations. In their case, the regional model predicted a much larger decrease, but this is in all likelihood because their region of study lies to the south of the region under discussion here.

c. *Hydroclimatological changes*

Figure 8 shows net precipitation (precipitation minus actual evapotranspiration), averaged over the entire year (left) and the summer months only (right). The climatological values for the validation period are shown (top) along with the climate change signal (bottom).

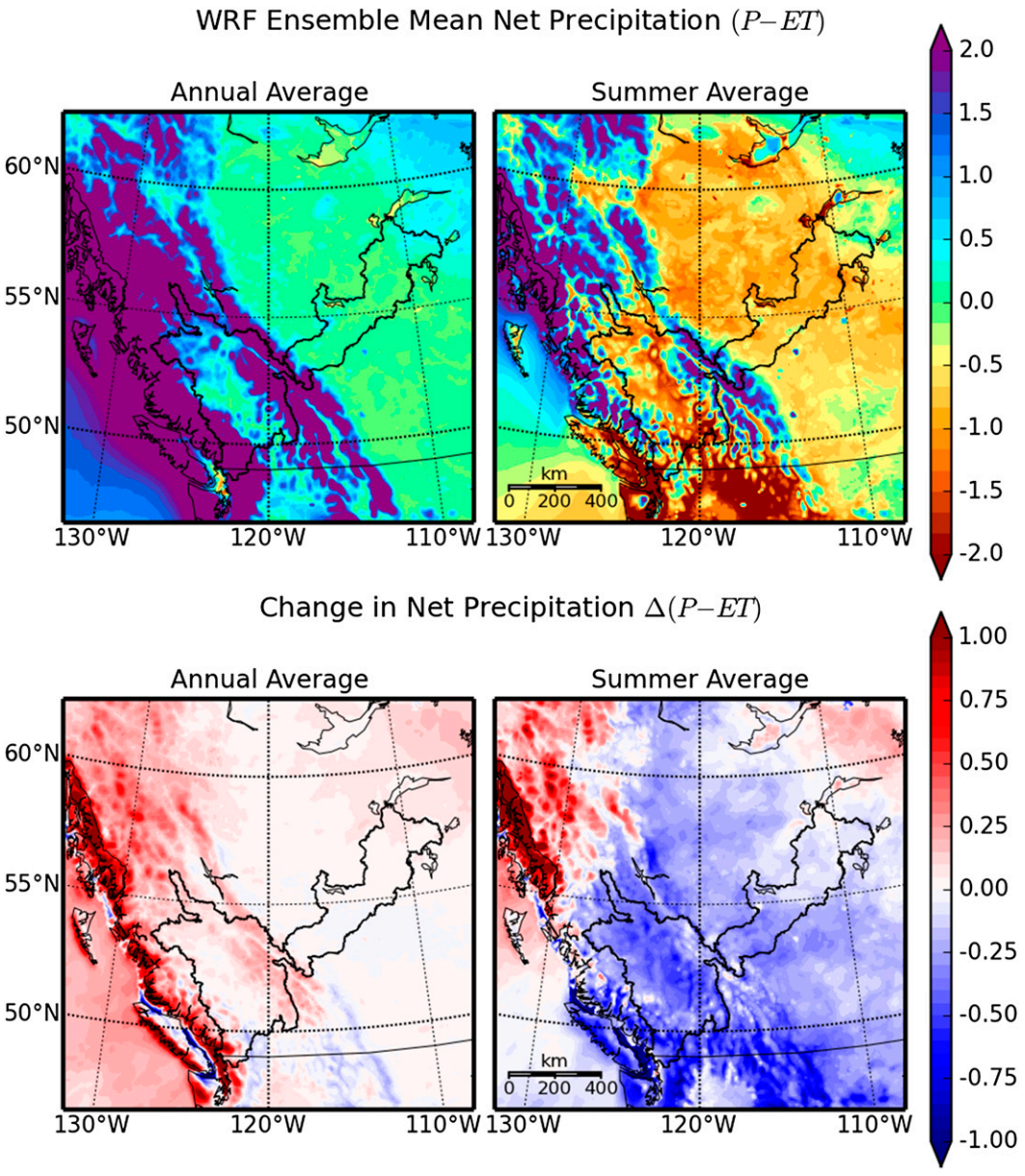

FIG. 8. Net precipitation (precipitation minus evapotranspiration; mm day^{-1}) for WRF ensemble mean (inner domain): (left) annual average and (right) summer average, showing values for (top) the historical period and (bottom) differences between projection and validation period.

Only the mountainous regions near the coast receive large amounts of excess precipitation, and most of the precipitation forms runoff, while only about 35% of the annual precipitation over the Fraser River basin evaporates. The continental regions, on the other hand, have much smaller net precipitation and higher evapotranspiration (ET). The annual ET rate over the Athabasca River basin is about 70% of the total precipitation, but this number is dominated by the mountainous part of the ARB, where the ET rate is 50% of precipitation. In the drier lowland sections of the basin it is almost 95%! (See the green areas in Fig. 8, top left.) Furthermore, during the summer season (top right) ET over the entire continental area in the rain shadow of the Rocky Mountains exceeds precipitation, which implies that ET is supplied by water that is stored in the soil and recharged in the cold season. (The regions of negative annual net precipitation are large lakes and coastal waters.) The fact that the water budget in the lee of the Rocky Mountains is close to balance (i.e., the runoff fraction is small), indicates that in these regions ET is limited by soil moisture availability, and recycling of precipitation plays an

important role in summer. The implied recycling rate averaged over both sides of the Rocky Mountains is consistent with the estimated global average (~70%; Trenberth et al. 2007), but the contrast between the windward and leeward side in our simulations is significantly larger than in previous estimates for this region, which were derived from lower resolution global climate models and reanalysis (Trenberth 1999; Anderson et al. 2009). It should, however, be noted at this point that evapotranspiration in WRF is computed by the relatively simple Noah LSM and the soil layer available for water storage is only 2 m deep.

The change in net precipitation (runoff generation) in the lee of the Rocky Mountains and the interior plateau is small: evaporative demand increases with the thermodynamic limit, while precipitation in our projections increases less than that, so that an even higher fraction of the additional precipitation evaporates. In the mountains, however, in particular near the coast and in higher latitudes, net precipitation does increase much like total precipitation (cf. Fig. 7). In summer the water deficit that was already apparent during the historical period increases everywhere and net summer precipitation only increases in the Coast Mountains north of 55°N (especially the part of the Coast Mountains located in Alaska; see appendix B for details).

The results shown in Fig. 8 suggest that summers in the lowlands east of the Rocky Mountains could become considerably drier. Note, however, that the increase in actual evapotranspiration in summer only reflects the increase in precipitation in the cold season, and is only indirectly an indication of increased evaporative demand. If the increased evaporative demand cannot be met, the soil dries out and actual evaporation drops. But because the Noah LSM has no representation of groundwater processes beyond 2-m depth, it is difficult to assess to which extent soil moisture would actually become a limiting factor. For a more comprehensive picture of hydrological conditions, an analysis of the seasonal cycle on a basin scale is necessary, which will be discussed in the next section (section 4).

Gutmann et al. (2012) analyzed very high-resolution regional climate simulations at a resolution of 2 and 4 km over Colorado, also using WRF. The climate of Colorado is similar to that of Alberta, in that the plains of Colorado lie in the rain shadow of the Rocky Mountains, and streamflow is primarily fed by seasonal snowmelt. Gutmann et al. (2012) also performed pseudo–global warming experiments, where only the temperature and humidity in the forcing fields were increased, but they did not perform simulations driven by fields from a dynamically consistent GCM. In these pseudo–global warming experiments they find that the increase in evapotranspiration exceeds the increase in precipitation, even though the latter was almost at the thermodynamic limit. However, in the projections presented here, precipitation increases are generally below the thermodynamic limit, even for orographic precipitation.

4. Basin-scale hydrological impacts

Figures 9 and 10 describe the seasonal cycle of hydroclimatic variables in the Fraser River basin (FRB) and the Athabasca River basin (ARB). Temperature variables were averaged and flux variables were integrated over the respective basin areas; all variables were also averaged over each 15-yr simulation period. The solid lines are ensemble averages for the mid-twenty-first-century projection period, dashed lines show the historical validation period, and the filled dots represent the merged gridded observations (only minimum, maximum, and mean temperatures and total precipitation are available) and the observed river discharge of the Fraser and Athabasca Rivers (lower right panel of Figs. 9 and 10, respectively). The minimum and maximum temperatures (top left) are daily minima and maxima of 2-m air temperature (i.e., the diurnal range). The net precipitation (bottom left) is defined as total precipitation minus actual evapotranspiration, and the net (surface) water flux (bottom right) is the net liquid precipitation plus snowmelt minus evapotranspiration (i.e., the net water input into the land model).[3] The total runoff (bottom right) is the amount of precipitation taken up by the land model and not returned to the atmosphere (i.e., water that is lost to surface runoff or groundwater; underground runoff).

Surface runoff is the component of runoff that does not infiltrate into the ground and directly contributes to streamflow. The land model calculates all runoff quantities separately for every grid point, and the seasonal cycle of basin integrated surface runoff does not include effects associated with river routing, such as travel time to the basin exit point. When comparing modeled surface runoff with observed river discharge, one should also keep in mind that a significant contribution to river discharge can also come from underground runoff through groundwater flow. This effect is not captured in a simple column-based land model such as Noah, and requires three-dimensional hydrological modeling. See

[3] In principle, the annual mean of net precipitation and net surface water flux should be the same; however, this is not the case here because of inconsistencies between the lake model and the land surface model.

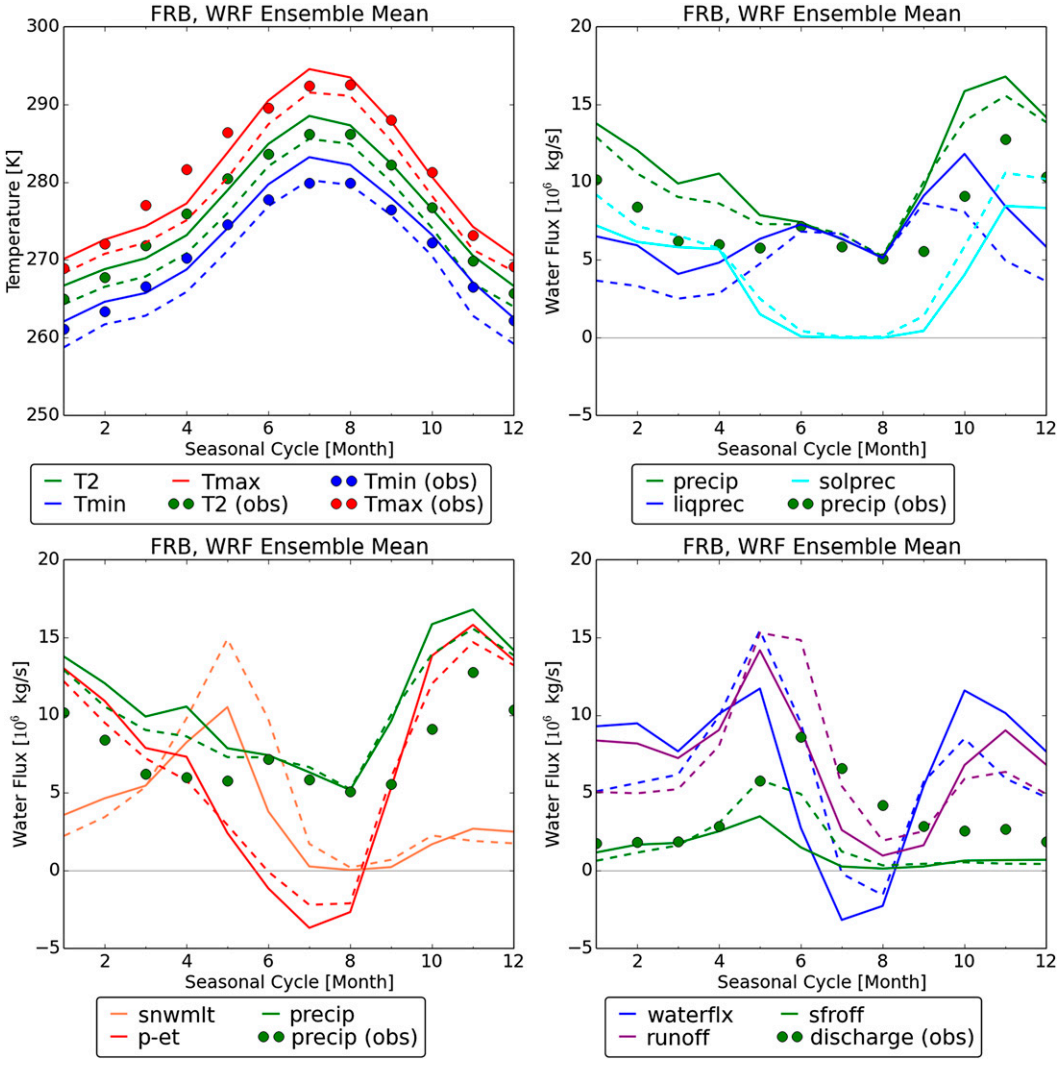

FIG. 9. Average seasonal cycle over the Fraser River basin: (top left) avg, min, and max 2-m air temperature; (top right) total, liquid, and solid precipitation; (bottom left) precipitation, snowmelt, and net precipitation; and (bottom right) total and surface runoff, net surface water flux, and Fraser River discharge. Temperatures are averaged and all other quantities are integrated over the entire basin. The mid-twenty-first-century projection period is shown with solid lines, the historical validation period with dashed lines, and observed values are indicated with filled circles.

appendix A (and Fig. A1) for a discussion of the relationship between modeled surface runoff and observed river discharge.

a. The Fraser River basin

The Fraser River basin is located directly east of the Coast Mountains, extends eastward to the Continental Divide, and drains through the Fraser River into the Pacific Ocean (near Vancouver). The Fraser River headwaters are located on the western slopes of the Rocky Mountains. Note that the western slopes of the Coast Mountains are not part of the FRB, and instead drain directly into the Pacific Ocean.

Figure 9 describes the seasonal cycle of hydroclimatic variables over the FRB. It is evident that the temperatures are generally too cold (by 2.8°C), and the (winter) precipitation is too high (by about 30%) compared to observations. The seasonal cycle in temperature is quite well reproduced, except for an even larger cold bias in spring (cf. section 3a). The seasonal cycle in precipitation is too strong, owing largely to excessive winter precipitation (the wettest season), while summer precipitation is simulated very accurately. The winter precipitation bias can partly be explained by an underestimation of the rain shadow effect discussed in section 3a. The precipitation deficit over the relevant section of the Pacific

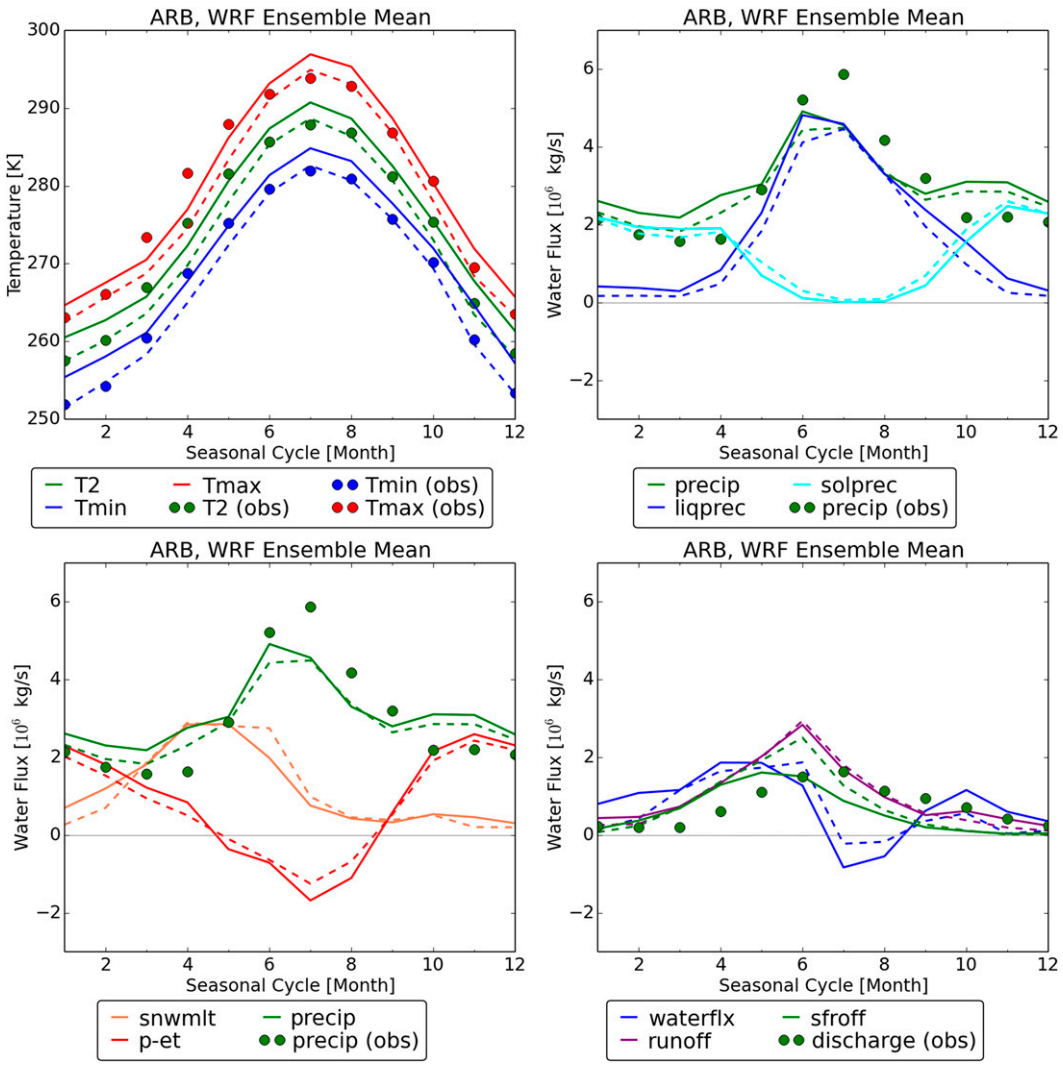

FIG. 10. As in Fig. 9, but for the Athabasca River basin. Note different axis scaling from Fig. 9.

seaboard (Vancouver Island and the Coast Mountains) can account for approximately 50% of the excess over the FRB (see appendix B for details).

The partitioning between liquid and solid precipitation during the winter is fairly even (Fig. 9, top right) and there is, unsurprisingly, virtually no solid precipitation in summer. During the late summer evapotranspiration exceeds precipitation, and the basin experiences a net water loss. Surface runoff clearly follows the timing of the snowmelt (Fig. 9, bottom), but this is due to limitations of the Noah land surface model, which cannot account for groundwater contributions to river flow. These groundwater contributions, although largely also meltwater, add to the total river discharge and delay the timing of peak flow by about one month (cf. Fig. 9, bottom right).

The mean temperature in the FRB is projected to increase by 2.4°C by midcentury, and annual precipitation by 4.5%. The major change in the hydrological cycle of the FRB will be the shift from solid to liquid precipitation in winter, which in turn will lead to a decline in snowmelt (Fig. 9, bottom left), and at the same time higher temperatures will also result in earlier snowmelt, which may increase (surface) runoff during the cold season. This finding is consistent with Salathé et al. (2010), who report a reduction in spring snowpack by the mid-twenty-first century for the state of Washington, immediately to the south. Pollock and Bush (2013), on the other hand, report an increase in snowfall for their mid- twenty-first-century time slice (2045–50), but Pollock and Bush (2013) chose to use a very optimistic emission scenario. The time slice that can be most accurately compared with our projection period (2045–60) in terms of radiative forcing, is their 2070–80 time slice, which does indeed also show a significant reduction in snowfall, consistent with our results.

Shrestha et al. (2012) comment that most CMIP3 GCMs predict a decrease in summer precipitation for the FRB, which is also the case for CESM in our simulations, but not for WRF (cf. Fig. 7, center). However, considering the far superior representation of summer precipitation in WRF (as opposed to CESM), we suggest that this may in fact be an artifact of the low resolution employed in GCMs. Furthermore, Shrestha et al. (2012) report that in the late summer season actual evapotranspiration is projected to drop, while potential evapotranspiration continues to rise, which would be indicative of soil moisture limitation. This is not the case in the simulations presented here. During both the historical and projection periods, actual evapotranspiration essentially follows potential evapotranspiration (not shown). However, this could at least partly be a consequence of excessive winter precipitation (because of moisture retention in the soil), and thus not be physically realistic.

From our results, based on the idealized study of Das et al. (2011), one can infer increased streamflow in the cold season due to reduced solid precipitation and earlier snowmelt, and reduced streamflow in the warm season due to increased evapotranspiration. The reduction in annual streamflow associated with warming will likely be offset by increased winter precipitation, so that the primary impact on the Fraser River discharge will be a change in the seasonal cycle: higher discharge in winter, lower in summer, and considerably lower peak flow in spring. The reason for the streamflow reduction in summer is more apparent if one considers changes in net water flux (Fig. 9, bottom right), which also accounts for changes in snowmelt, rather than net precipitation alone. Historically, net water loss to the atmosphere in summer was largely compensated by late snowmelt, but by mid- twenty-first-century summer snowmelt is projected to drop significantly, thereby increasing the water deficit of the land surface model. This means less water will be available to supply late summer streamflow. The surface runoff generated by the Noah LSM (and shown in Fig. 9, bottom right) qualitatively supports this conclusion. However, groundwater processes, which are not captured in the Noah land model, strongly affect late summer river flow so that this conclusion would be premature. Application of a comprehensive hydrological model will be required to resolve this question.

Such a hydrological model was employed by Shrestha et al. (2012) and Kerkhoven and Gan (2011) to simulate historical and future streamflow in the FRB. The main limitation of both studies, however, is that they only employed bias-corrected GCM output, which cannot account for local feedback effects. Nevertheless, their conclusions are consistent with those presented here, in that both report a strong reduction in the snowmelt-driven seasonal peak flow, but no significant net change in the average annual flow.

b. *The Athabasca River basin*

In contrast to the FRB, the Athabasca River basin is located to the east of the Continental Divide, though the Athabasca River headwaters are also in the Rocky Mountains, just to the east of the Fraser River headwaters. The ARB drains into Lake Athabasca, which eventually drains into the Arctic Ocean, through the McKenzie River system, of which it is a part. Note that the ARB covers a smaller area than the FRB and the average precipitation rate is much lower, so that the basin-integrated water flux is much smaller.

The hydroclimatic variables for the ARB are shown in Fig. 10. The seasonal cycle of temperature, including the diurnal range, is evidently captured very well in the WRF simulations, except for a cold bias in spring. The annual temperature bias is −1.4°C. The seasonal cycle of precipitation is somewhat underestimated in that late summer precipitation is too low and winter precipitation is too high. The outer domain and the global model are characterized by a progressively weaker seasonal cycle, with more precipitation in winter, and less in summer (not shown). Even though the higher winter precipitation is again likely due to the rain shadow effect (as discussed above), the annual total precipitation over the basin is within 1% of the observations.

Most of the precipitation in winter falls in solid form, which leads to a snowmelt peak in late spring and once more (surface) runoff closely follows snowmelt. In observations as well as in our simulations, total precipitation does in fact peak in summer, but because most of the precipitation is lost to evapotranspiration, net precipitation is negative throughout the entire summer, and runoff generation is small. Net water input into the ARB thus primarily occurs during the cold season and is stored in the snowpack (and to some extent in the soil). These conclusions are of course based on simulations, and observations of water storage in the snowpack would be necessary to assess their accuracy. Further note that the apparent increase in net precipitation in late summer is associated with a decrease in evapotranspiration (since precipitation also decreases). The decrease in evapotranspiration appears to be due to soil moisture limitation, because potential evapotranspiration continues to be high during that time (not shown).

On average, the observed discharge of the Athabasca River peaks in July, and maintains relatively high flow rates until late fall (cf. Fig. 10, bottom right). The (surface) runoff peak appears slightly too early in our simulations and the flow is not maintained throughout the summer. This, however, is easily explained by the missing groundwater flow component in the Noah LSM, which

would delay the annual peak flow and supply water until much later in the year (cf. section 4a and appendix A for a discussion of the effect of groundwater flow).

The projected warming in the ARB by the mid-twenty-first century is 2.2°C and the annual precipitation increase is projected to be 6.5%, where most of the increase occurs in winter precipitation. Unlike the case of the FRB, the partitioning between solid and liquid precipitation does not change appreciably because of the continental climate of the ARB (i.e., lower winter temperatures). However, increasing temperatures lead to earlier snowmelt and significantly increased evapotranspiration in summer. In contrast to Kerkhoven and Gan (2011), we do not find evidence for significantly increased sublimation from snow, but instead most of the (increasing) evaporative losses occur during and after the melt season.

Again, based on the idealized results of Das et al. (2011), one can expect an earlier onset of the spring freshet and increased streamflow in the cold season by the mid-twenty-first century as well as a reduction in warm season streamflow, in particular in late summer (cf. net water flux at the surface as in Fig. 9, bottom right). Compared to the FRB, however, the increased net water loss to the atmosphere in summer is more driven by actual evapotranspiration, while the change in late season snowmelt is less significant. As in the FRB, the modest increase in winter precipitation will likely offset the reduction in annual average streamflow because of increased evaporative losses. But in lieu of results from a coupled hydrological model capable of accurately representing subsurface groundwater flow, this conclusion must still be seen as somewhat speculative. Without groundwater processes, large parts of the basin are constrained by local water conservation, so that net precipitation cannot increase, as long as the evaporative demand is sufficiently high (cf. section 3c). In this context, it is also unclear how much streamflow from higher elevations would reenter the soil during dry periods and subsequently be lost to the atmosphere through plant transpiration and again contribute to precipitation (nonlocal precipitation recycling; cf. van der Ent and Savenije 2011). Kerkhoven and Gan (2011) do in fact report a consistent reduction in late summer streamflow, although several of their simulations also show increased peak flow due to increased snowmelt, which is not consistent with our results.

5. Natural variability

Natural variability, especially on regional scales, is a major uncertainty in climate projections; in fact, on regional scales it is estimated to be of similar magnitude to model uncertainty (Hawkins and Sutton 2009; Deser et al. 2012a; Knutti et al. 2008).

a. Natural variability on a basin scale

To illustrate the magnitude of natural variability on the basin scale we show components of the surface water budget for all four WRF ensemble members separately; for the FRB in Fig. 11 and the ARB in Fig. 12. Note that each ensemble member is still averaged over the entire 15-yr simulation period and the respective river basin, but no ensemble averaging has been performed. Essentially, each one of the panels shows a plausible mean climatology for a historical and future period of 15 yr. It is useful to reemphasize that the only differences between the ensemble members are the initial conditions from which the global model projections were initialized; the configurations of the global and regional models and the forcing scenario are identical between all ensemble members. The largest variability among ensemble members is seen in snowmelt over the FRB. While two ensemble members (on the left) start out with high volumes of snowmelt and subsequently experience a dramatic reduction, the other two ensemble members begin with a smaller volume and experience only very little change by the mid-twenty-first century. Large reductions in spring snowmelt are also associated with warmer spring temperatures. The amount of snowmelt is, of course, equal to the amount of solid precipitation, and there is a positive feedback between warmer winter and spring temperatures and less solid precipitation resulting from the influence of snow albedo, which may amplify the differences between ensemble members.

In the ARB the same two ensemble members that predict less snowmelt in the FRB predict higher summer evaporation and earlier snowmelt (less snowmelt in late spring), while the other two ensemble members again predict less change in snowmelt and net precipitation. The association between spring temperatures and snowmelt also holds in the ARB, and in addition, earlier snowmelt also appears to be associated with an earlier peak in summer precipitation.

It is worth noting that both Shrestha et al. (2012) and Kerkhoven and Gan (2011) report differences on the order of 10%–20% in annual and seasonal streamflow between simulations forced with output from different GCMs. In the light of this discussion it is likely that at least some of the variance can be attributed to natural (internal) variability within each GCM, as opposed to systematic differences between the models.

These results clearly illustrate the dangers of using the delta method with only one model integration. Because of natural variability in both, the historical and the future climate, the variability/uncertainty in the climate change signal becomes even larger. It is interesting that, especially in the FRB, the realizations with the highest

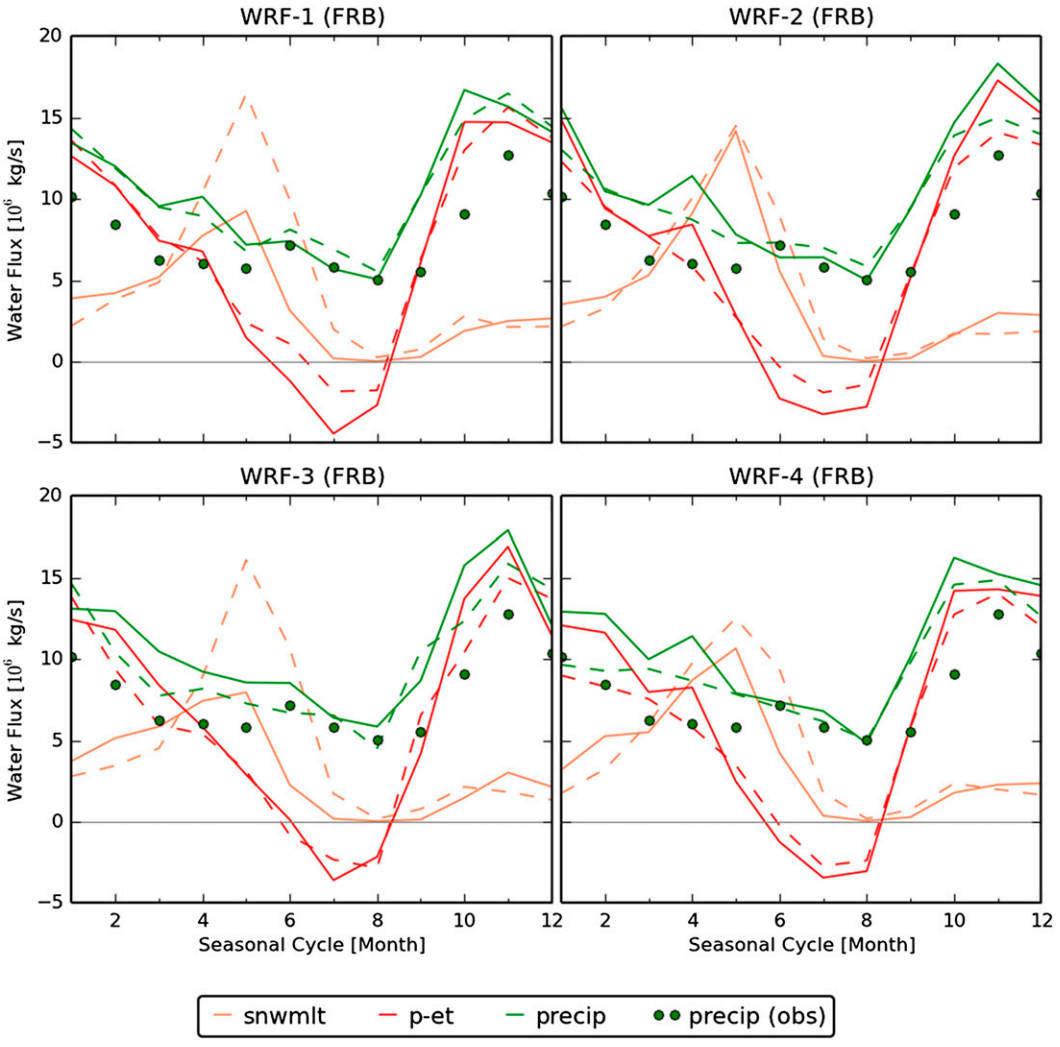

FIG. 11. The seasonal cycle of total and net precipitation as well as snowmelt, averaged over the Fraser River basin, for all four WRF ensemble members (inner domain). Each ensemble member was averaged over its entire 15-yr simulation period. All panels are analogous to the bottom-left panel of Fig. 9.

positive bias turn out to be the ones with the largest change signal (in the opposite direction). But of course the size of the ensemble is too small to permit any conclusions to be drawn on the basis of this observation.

Finally we note that the deviation of each ensemble member from the ensemble mean, as well as the sign of the change between the historical and the future periods, is almost identical to those in the 15-yr climatologies, if the average is only taken over 10 yr. This suggests that the differences between ensemble members are primarily driven either by large-scale modes of decadal (or longer) variability imposed by the global model, or that there are multiple equilibria in surface climate that are stable over decadal time scales. Sensitivity tests have shown that differences between ensemble members are larger than differences between model runs with the same boundary forcing but using slightly different model configurations, which suggest that large-scale decadal variability imparted by the global model is the dominant effect. However, internal feedback processes, such as snow albedo and precipitation recycling, can amplify the response to external forcing.

b. *The influence of large-scale variability*

To investigate the influence of large-scale variability on the basin-scale climate, several common indicators of climate variability in the region of interest have been computed (see section 2d for details). Table 1 lists the average values for the NPO, NPI, Niño-3.4 ENSO index, AMO, NAO, NAM, PDO, and PNA. All indices were derived from the CESM simulations and averaged over the simulation period of each ensemble member; the

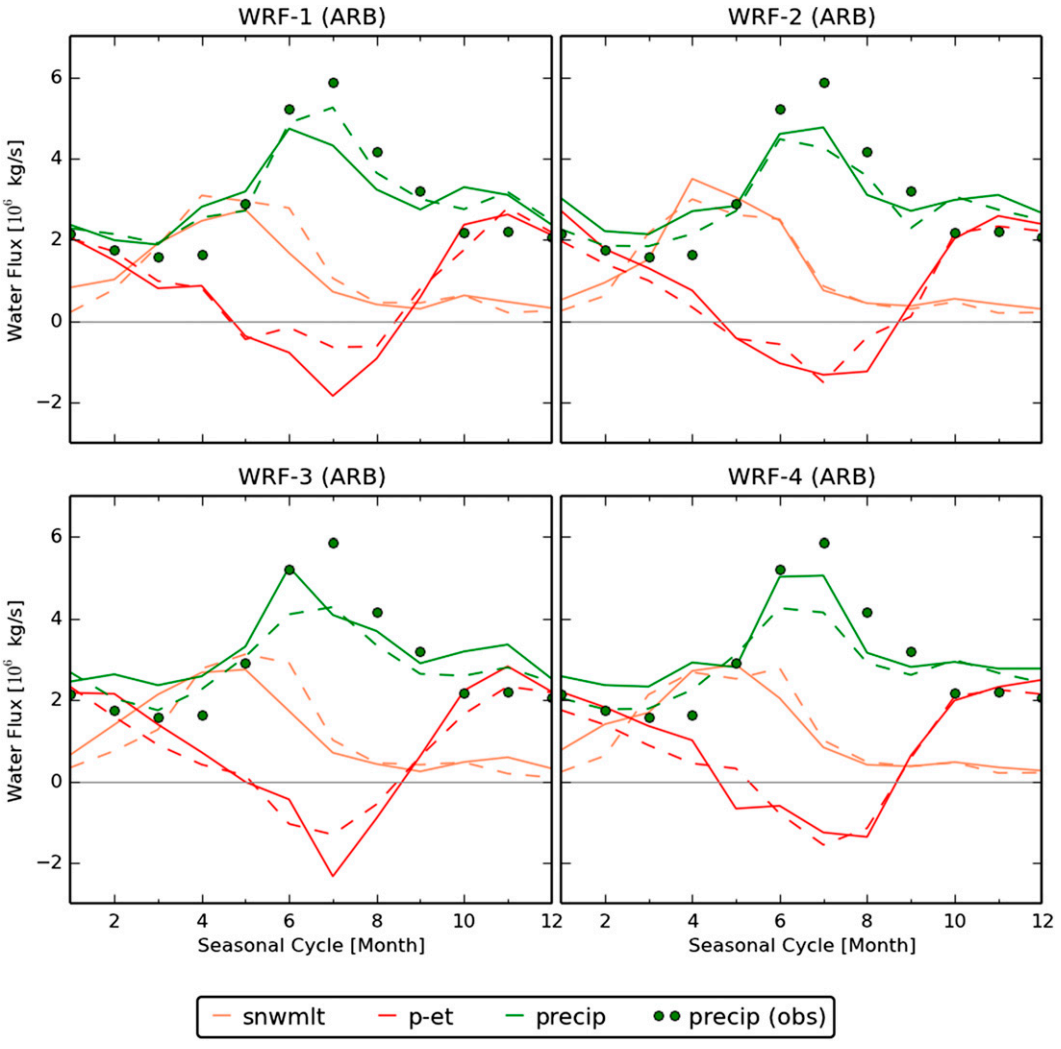

FIG. 12. The seasonal cycle of total and net precipitation as well as snowmelt, averaged over the Athabasca River basin, for all four WRF ensemble members (inner domain). Each ensemble member was averaged over its entire 15-yr simulation period. All panels are analogous to the bottom-left panel of Fig. 10.

observed indices were derived from observational datasets and averaged over the historical validation period (1979–94). For CESM the values for the validation period and the differences ("Delta") to the projection period are shown. The latter can shed some light on the differing trends seen in the ensemble members, where the largest differences between ensemble members occur for the North Pacific index and the PDO. Note, however, that there is no a priori reason that Pacific modes of variability should dominate the differences between ensemble members, as these indices are derived from a global model/dataset. The reason for this coincidence is likely that the characteristic time scale of these two modes is similar to the simulation period of our ensemble (decadal). The AMO index is effectively invariant between ensemble members, because the AMO signal is only very poorly captured in the simulations and the analysis period is too short to characterize variability on a multidecadal time-scale. The PDO pattern, on the other hand, is reproduced very well in CESM. Figure 13 shows the SST pattern associated with the PDO for the observational record as well as for the CESM ensemble. Note that the PDO pattern obtained from concatenating only four 15-yr simulations is exceedingly similar to the pattern obtained by Deser et al. (2012b) from their 1300-yr preindustrial control simulation.[4]

[4] The sign convention adopted for this analysis is such that the SST anomaly pattern shown in Fig. 13 is defined as the positive phase of the PDO (which is the inverse of the conventional definition).

TABLE 1. Values for several indices of climate variability for each CESM ensemble member as well as for observations, averaged over the historical validation period. For CESM the changes in the future projection period with respect to the validation period are also given (i.e., Delta). Deviations close to ±0.3 and larger are emphasized in boldface.

Experiment	NPO	NPI	Niño-3.4	AMO	NAO	NAM	PDO	PNA
Observations	+0.12	**−0.84**	+0.17	−0.18	+0.17	+0.16	**−0.59**	+0.12
CESM Exp 1	−0.05	+0.01	−0.20	+0.00	−0.00	+0.01	+0.10	−0.02
CESM Exp 2	+0.04	**−0.68**	+0.16	+0.01	−0.12	−0.07	**−0.37**	+0.11
CESM Exp 3	+0.13	**+0.73**	−0.00	−0.00	+0.12	+0.18	**+0.35**	−0.16
CESM Exp 4	−0.12	+0.04	+0.04	−0.01	+0.00	−0.12	−0.07	+0.07
Exp 1 Delta	+0.03	**−1.41**	**+0.29**	+0.01	+0.07	−0.06	**−0.63**	+0.18
Exp 2 Delta	+0.12	**+1.44**	−0.22	−0.01	+0.13	+0.22	**+1.19**	−0.23
Exp 3 Delta	−0.26	−0.17	+0.04	−0.00	−0.22	−0.25	**−0.38**	+0.11
Exp 4 Delta	+0.11	−0.08	−0.11	+0.00	+0.02	+0.10	−0.18	−0.06

Closer examination of the Deltas in Table 1 shows that it is often ensemble member (Exp) 2 that differs from the other ensemble members, in particular in the phases of NPI, PDO, and PNA. Furthermore, Exp 1 tends to be on the extreme opposite end compared to Exp 2 (and is the only one with an appreciably positive Niño-3.4 index).

It is useful to discuss the degree to which these differences can explain the different hydroclimatic trends found in section 5a. To this end, Table 2 summarizes the time series correlations of the aforementioned climate indices with winter precipitation and spring temperature averaged over the two basins (FRB and ARB) for observational data (from CRU and GPCC) and WRF (inner domain only). In the observations, spring temperature and to a somewhat lesser extent winter precipitation correlate with the NPI and PDO as well as with the PNA. In WRF, however, only the temperature correlations with the NPI and with the PDO over the FRB survive. Precipitation in the inner WRF domain does not correlate significantly with any of the large-scale climate indices. The correlation with the AMO that appears over the ARB is likely spurious, since the AMO characteristics are not adequately captured.

Winter precipitation and spring temperature are highly relevant for spring snowmelt, in which the largest differences between ensemble members are apparent. However, snowmelt in WRF only shows a correlation with the NPI and PDO in some months, such that a positive phase leads to later snowmelt, but the correlation is weak (~0.4) and unstable between periods. Precipitation and temperature in other seasons do not strongly correlate with large-scale climate indices. The only exception is a correlation of summer temperature over the FRB with the Niño-3.4 index (i.e., ENSO; ~0.6) in both observations and the model ensembles.

The high correlations with temperature in observations may partially be explained by the fact that some indices project on the global warming trend, so that the longer continuous time series would lead to a higher correlation. However, there is no strong trend in precipitation that could explain this difference between observations and our WRF simulations. Finally, we note that these correlations are not consistent between WRF and CESM; in particular, temperature and precipitation in CESM correlate more strongly with ENSO, and less so with the PDO.

We conclude that the NPI and PDO, which are also highly correlated with one another (~0.75), explain a large part of the differences between the ensemble members, in

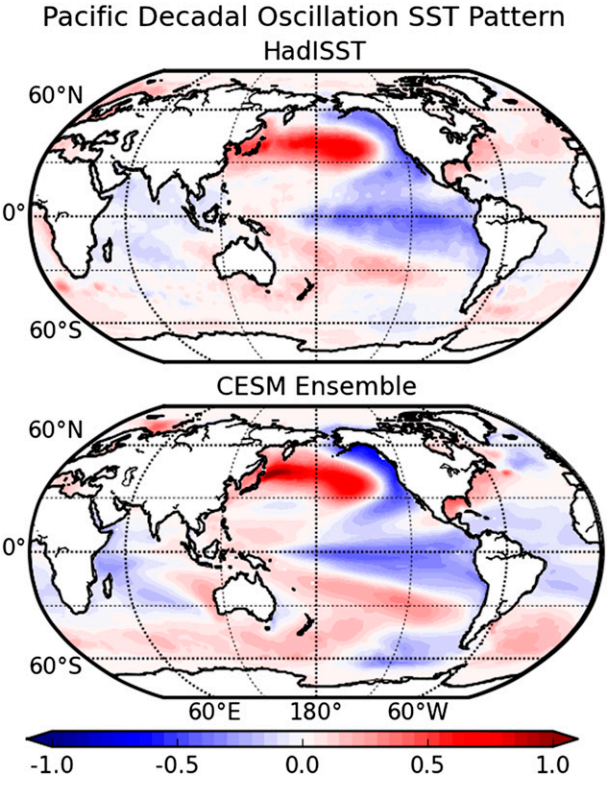

FIG. 13. The SST pattern associated with the PDO obtained from (top) the observational record and (bottom) the concatenated CESM ensemble. The global pattern is obtained by regressing monthly SST anomalies against the PDO time series; the explained variance is 20% in both model and observations.

TABLE 2. Correlation coefficients of the climate indices from Table 1 (rows) with winter precipitation (P_{DJF}) and spring temperature (T_{MAM}) over the Fraser and Athabasca River basins (columns); for the observational record and for the WRF ensemble (inner domain). Correlation coefficients close to ±0.5 and larger are emphasized in boldface.

	Observations (GPCC and CRU)				WRF (inner domain)			
	FRB		ARB		FRB		ARB	
Index	P_{DJF}	T_{MAM}	P_{DJF}	T_{MAM}	P_{DJF}	T_{MAM}	P_{DJF}	T_{MAM}
NPO	−0.15	+0.16	−0.41	+0.28	−0.04	+0.05	+0.11	+0.43
NPI	**+0.53**	**−0.71**	**+0.57**	**−0.69**	−0.16	**−0.64**	−0.08	**−0.52**
Niño-3.4	−0.32	+0.42	−0.37	+0.19	−0.35	−0.05	−0.37	−0.28
AMO	−0.09	−0.13	−0.06	−0.25	+0.14	+0.38	+0.18	**+0.50**
NAO	+0.13	−0.05	+0.01	−0.12	−0.16	−0.20	−0.11	+0.20
NAM	+0.10	+0.00	−0.05	−0.04	−0.07	−0.13	+0.04	+0.41
PDO	**+0.48**	**−0.71**	**+0.55**	**−0.56**	+0.28	**−0.53**	+0.25	−0.21
PNA	**−0.48**	**+0.67**	**−0.54**	**+0.63**	+0.08	+0.41	−0.14	−0.15

particular with regard to snowmelt. But other climate modes also have an impact, and in the summer season smaller-scale internal variability is probably dominant.

6. Summary and conclusions

We have presented high-resolution regional climate projections for mid-twenty-first-century western Canada and analyzed hydrological impacts in the Fraser and Athabasca River basins. The fully coupled global climate model CESM was used to generate a small initial condition ensemble of climate projections for the RCP8.5 scenario, and the individual members of this ensemble were dynamically downscaled to a resolution of 10 km, using WRF with state-of-the-art physics parameterizations.

The regional model dramatically improves the representation of the seasonal cycle and the rain shadow effect of the Rocky Mountains. It captures the sharp contrast between the extremely wet maritime climate at the coast, which is dominated by orographic precipitation, and the dry continental climate in the lee of the Rocky Mountains. However, even at 10-km resolution the orographic precipitation at the first rain barrier (the Coast Mountains) is still underestimated, and subsequently precipitation in the rain shadow is overestimated; this effect is particularly pronounced in winter. As a consequence, regions in the rain shadow tend to have too much snow and also lower spring temperatures and later snowmelt. This limitation is almost certainly due to insufficient resolution of the topography and common in atmospheric models of this type. It can thus be argued that even higher resolution in the downscaling ''pipeline'' is liable to produce a significant further improvement in the quality of the results.

We further find that most of the precipitation in the lowlands east of the Rocky Mountains falls as convective precipitation in summer, which is largely recycled through local evapotranspiration. Furthermore, in our simulations net precipitation in summer is in fact negative, so that the net water input into the system actually occurs in the cold season (despite the precipitation maximum in summer). Most of the runoff is generated at higher elevations.

The mid-twenty-first-century projections show a modest increase in precipitation in all seasons (~5%), with an enhanced increase in spring (up to 10%). However, because of increased evaporative demand, net precipitation in summer is actually projected to decrease almost everywhere, except in the northern Coast Mountains and Alaska. An average warming of approximately 2.5°C is projected, with considerable amplification in the Polar Regions in winter and at high elevations in summer.

The most important projected change in the Fraser River basin is a shift from more solid to more liquid precipitation. The projected increase in annual net precipitation is only 4.5%, with fairly small variability between ensemble members; a warming of 2.4°C is projected. As a consequence, the seasonal snowpack is likely to shrink, but variability between ensemble members is large, possibly due to the effect of the snow–albedo feedback on spring temperatures. In the FRB the net effect is likely going to be a large reduction in the seasonal cycle of the streamflow, including a reduction in the meltwater-driven peak flow in early summer.

In the Athabasca River basin, on the other hand, annual net precipitation changes are more uncertain, with projected changes ranging from −20% to +20%, with the ensemble mean at 6.5%. This is partly because only a small part of the basin (in the mountains) actually has significant positive net precipitation. The projected warming is 2.2°C but, unlike in the FRB, the fraction of solid precipitation is unlikely to change because winters remain much colder on account of the continental climate. The most significant climate change impact in the ARB is most likely going to be a reduction in late

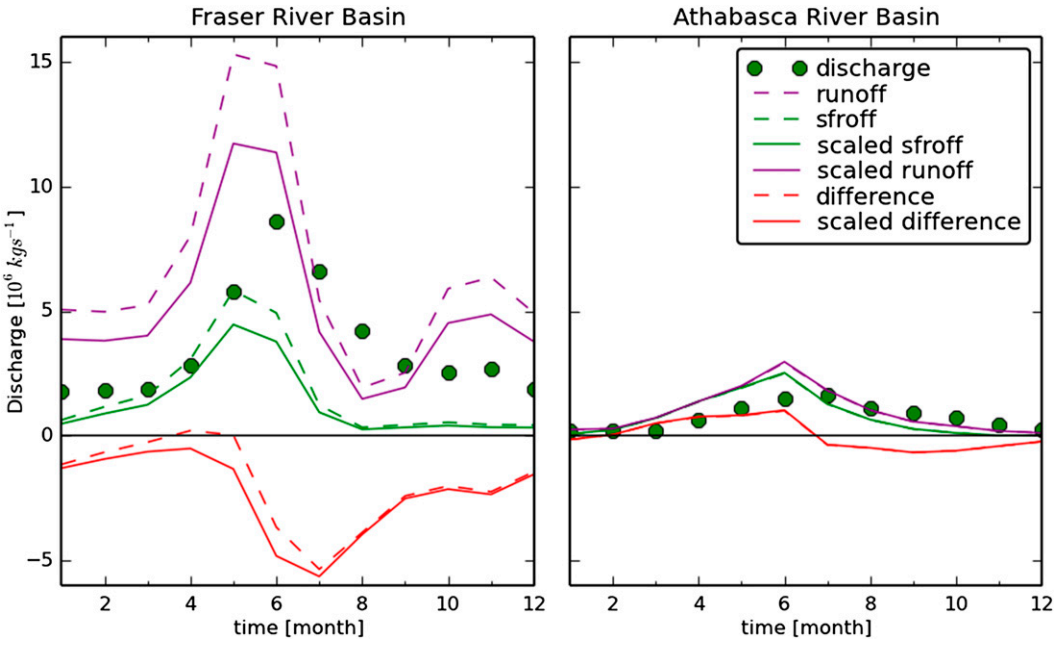

FIG. A1. The average seasonal cycle of total and surface runoff, observed river discharge, and the difference between surface runoff and observed discharge over the (left) Fraser and (right) Athabasca River basins. Bias-corrected values are shown with solid lines, direct WRF output with dashed lines, and observed discharge with filled circles.

summer runoff. There are also indications of a higher risk of drought in late summer, because of earlier snowmelt and increased evaporative demand, but at this point this must been seen as speculative.

A major uncertainty limiting the predictive power of the projections presented here is the magnitude of natural (internal) variability. The major climate change impacts in each basin appear to be most subject to variability, namely involving snowmelt volume in the FRB and net summer precipitation in the ARB. In particular, in each case, two out of four ensemble members show almost no change, while the other two show a strong trend (in the same direction). An analysis of large-scale variability suggests that the North Pacific index and the Pacific decadal oscillation (and in observations also the PNA) correlate with variables that control snowmelt.

This clearly underscores the need for a larger ensemble and the application of a probabilistic approach to interpretation. Had we only performed one of the four projections, we might have reported anything from no changes at all to a dramatic decrease in precipitation and extended drought in the ARB. A better understanding of the drivers of the variability would further inform the construction of a meaningful minimal ensemble, and aid in the interpretation of results.

Acknowledgments. The simulations presented in this paper were performed on the SciNet supercomputing center at the University of Toronto, which is a component of the Compute Canada HPC platform. The authors thank Dr. J. Gula for assistance with the initial setup of the modeling chain and Dr. D. Gruner and the SciNet team for assistance during the setup and operation of WRF. ARE was partially supported by a SOSCIP Graduate Student Fellowship, and MD was supported by a SOSCIP Post-doctoral Fellowship. The research of WRP is supported by NSERC Discovery Grant A9627.

APPENDIX A

The Impact of Subsurface Hydrology

In the discussion of hydrological changes in the Fraser and Athabasca River basins (section 4), we have pointed out the absence of a representation of subsurface hydrology in the Noah land surface model and discussed how this might affect the comparison between WRF surface runoff and actual river discharge. The mismatch between the surface runoff generated by the Noah LSM in WRF and the observed river discharge of the Fraser and Athabasca Rivers is shown in Fig. A1. The observed monthly mean discharge values from river gauging stations are shown in green circles, while uncorrected and bias-corrected model output is shown with dashed and solid lines respectively. The bias correction that was applied here is simply a scaling of total and surface

runoff with the ratio of observed to modeled annual mean precipitation over the respective basins. The correction was applied because the comparison of runoff with observed river discharge in the FRB is confounded by a significant bias. The correction is irrelevant for the ARB because the modeled annual precipitation is within 1% of the observed value. Surface runoff in the Noah LSM is the component of the downward water flux that does not infiltrate into the soil and is removed immediately. Total runoff is the total amount of water the land model ''loses,'' either at the bottom of the 2-m soil layer or through surface runoff (underground runoff + surface runoff). Surface runoff directly contributes to streamflow, and hence we compare modeled surface runoff with observed river discharge. It is, however, important to note that underground (subsurface hydrological) runoff also contributes to streamflow through groundwater flux into the river; this occurs predominantly in wet regions when the soil is saturated. The difference between the modeled surface runoff and the observed discharge can be seen as indicative of the role of subsurface hydrology. To the extent that surface runoff is modeled accurately in the Noah LSM and that travel time through the river system is small, the difference to the actual river discharge would have to be made up by groundwater flux into the river.

In both basins the large differences between modeled surface runoff and observed river discharge occur in the warm season. However, in the ARB differences are first positive, and then negative, whereas in the FRB the differences are negative throughout with varying magnitude. The significant and consistent negative difference implies that a large contribution to river discharge in the FRB in fact comes from groundwater flux into the Fraser River. In the Noah LSM this water is treated as underground runoff and is not included in surface runoff. The difference in the ARB appears in two phases. In spring and early summer surface runoff is larger than the average Athabasca River discharge, and in late summer and fall it is smaller. The reason for this is that snowmelt in the Noah LSM contributes to surface runoff immediately, but in reality some of the meltwater can infiltrate into the soil and contribute to streamflow later in the summer (cf. Kerkhoven and Gan 2011).[A1] This effect is likely also relevant in the FRB, where it can explain the seasonal modulation of the difference between modeled surface runoff and observed river discharge. In spring, snowmelt contributes to surface runoff and makes up for the missing groundwater contribution, while later in summer the missing subsurface component of meltwater adds to the missing background groundwater flux, and the difference between surface and river discharge becomes the largest.

In summary, in both basins the role of subsurface hydrology is to delay the contribution of meltwater to river discharge and to spread it out over the year, but in the FRB there also appears to be a significant contribution of groundwater flux to the total annual river discharge.

APPENDIX B

Precipitation Changes over the Pacific Seaboard

The Pacific seaboard (PSB) is a large area of coastal mountain ranges that drains directly into the Pacific Ocean. The area was arbitrarily divided at the 55th parallel to show the differing impacts of climate change on these two areas. The northern PSB encompasses all mountain ranges and basins along the Alaskan coast from the 55th parallel to the St. Elias Mountains. The southern PSB is comprised of the Canadian Coast Ranges south of the 55th parallel, the Queen Charlotte Islands, and Vancouver Island.

Figure B1 shows total and net precipitation, as well as snowmelt for the northern and southern PSB (as in Figs. 9 and 10, bottom left). It is evident that, unlike in the FRB and ARB, winter precipitation throughout the PSB is underestimated. The FRB lies partially in the rain shadow of the southern PSB, and during winter the amount of excess precipitation over the FRB is comparable to the amount that is missing over the southern PSB. But in fall and spring, when precipitation over the FRB is significantly overestimated, the simulated precipitation over the southern PSB is closer to observations, and cannot account for the precipitation excess. Total precipitation over the PSB is projected to increase by about 7% in the southern part and 10% in the northern part, with an average temperature increase of about 2.6° and 2.4°C, respectively (the PSB has a similar cold bias as the FRB; not shown). These increases clearly fall short of the thermodynamic limit of 7% $°C^{-1}$, but are also higher than the domain average (cf. section 3a). Whereas the precipitation increase over the northern PSB is relatively uniform throughout the year, the increase over the southern PSB is limited to the cold season.

A notable climatological difference between the northern and southern PSB is the significance if evapotranspiration, which is directly linked to temperature. In

[A1] Other factors that may contribute to larger runoff in the spring are a slight overestimation of precipitation in winter compared to summer, and the absence of very high elevations in the smoothed topography, which would contribute to surface runoff later in the year.

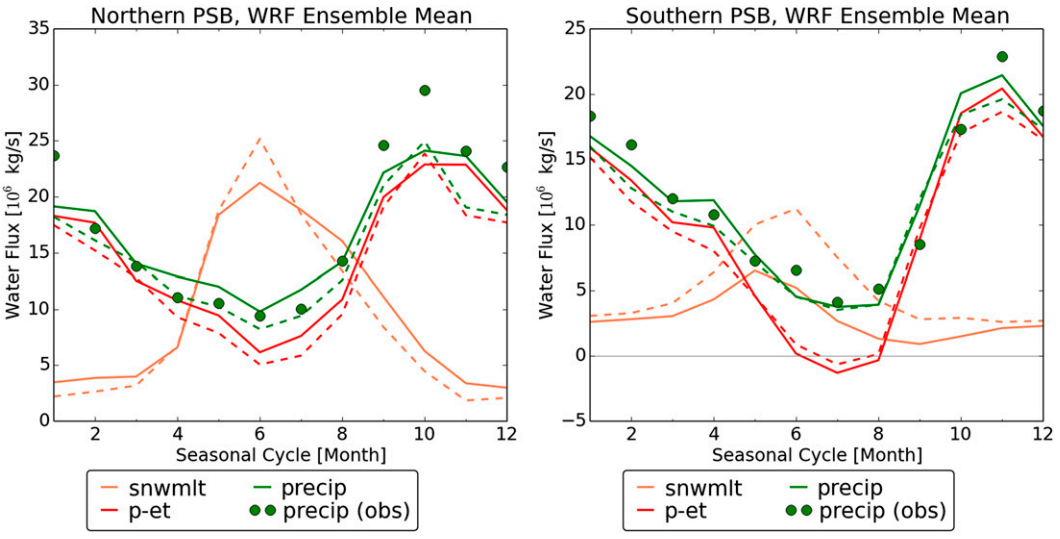

FIG. B1. The average seasonal cycle over the (left) northern and (right) southern PSB: precipitation, snowmelt, and net precipitation, integrated over the coastal mountain ranges north and south of the 55th parallel, respectively. Values for mid-twenty-first-century projection period are shown in solid lines, historical values in dashed lines; observed values are indicated with filled circles. Note different axis scaling from Figs. 9 and 10.

the northern part ET never exceeds precipitation, and the increase in summer precipitation is not outpaced by evapotranspiration (unlike in the ARB). In the southern part, however, net precipitation is slightly negative and this does not change significantly.

In terms of climate change impacts, the main difference between the northern PSB and the southern PSB is the change in snowmelt. While total snowmelt does not change significantly in the northern part, it decreases significantly in the southern part, due to a shift to more liquid precipitation in winter (not shown). At the same time surface runoff in the PSB is largely driven by snowmelt. The effect in both regions will be that surface runoff and snowmelt become more evenly distributed over the year, but while the northern PSB will retain the large volume of spring melt, the southern PSB will likely lose most of its snowmelt-driven peak runoff during the melt season (and total surface runoff might decrease).

The conclusions regarding surface runoff and streamflow are, of course, subject to the same caveats outlined in section 4 and appendix A.

REFERENCES

Anderson, B. T., A. C. Ruane, J. O. Roads, and M. Kanamitsu, 2009: Estimating the influence of evaporation and moisture-flux convergence upon seasonal precipitation rates. Part II: An analysis for North America based upon the NCEP–DOE Reanalysis II model. *J. Hydrometeor.,* **10,** 893–911, doi:10.1175/2009JHM1063.1.

Arritt, R. W., and M. Rummukainen, 2011: Challenges in regional-scale climate modeling. *Bull. Amer. Meteor. Soc.,* **92,** 365–368, doi:10.1175/2010BAMS2971.1.

Burn, D. H., 2008: Climatic influences on streamflow timing in the headwaters of the Mackenzie River Basin. *J. Hydrol.,* **352,** 225–238, doi:10.1016/j.jhydrol.2008.01.019.

Cassano, J. J., M. E. Higgins, and M. W. Seefeldt, 2011: Performance of the Weather Research and Forecasting Model for month-long pan-Arctic simulations. *Mon. Wea. Rev.,* **139,** 3469–3488, doi:10.1175/MWR-D-10-05065.1.

Compo, G. P., and Coauthors, 2011: The Twentieth Century Reanalysis Project. *Quart. J. Roy. Meteor. Soc.,* **137,** 1–28, doi:10.1002/qj.776.

Daly, C., M. Halbleib, J. I. Smith, W. P. Gibson, M. K. Doggett, G. H. Taylor, J. Curtis, and P. P. Pasteris, 2008: Physiographically sensitive mapping of climatological temperature and precipitation across the conterminous United States. *Int. J. Climatol.,* **28,** 2031–2064, doi:10.1002/joc.1688.

Danabasoglu, G., S. C. Bates, B. P. Briegleb, S. R. Jayne, M. Jochum, W. G. Large, S. Peacock, and S. G. Yeager, 2012: The CCSM4 ocean component. *J. Climate,* **25,** 1361–1389, doi:10.1175/JCLI-D-11-00091.1.

Das, T., D. W. Pierce, D. R. Cayan, J. A. Vano, and D. P. Lettenmaier, 2011: The importance of warm season warming to western U.S. streamflow changes. *Geophys. Res. Lett.,* **38,** L23403, doi:10.1029/2011GL049660.

Deser, C., A. Phillips, V. Bourdette, and H. Teng, 2012a: Uncertainty in climate change projections: The role of internal variability. *Climate Dyn.,* **38,** 527–546, doi:10.1007/s00382-010-0977-x.

——, and Coauthors, 2012b: ENSO and Pacific decadal variability in the Community Climate System Model version 4. *J. Climate,* **25,** 2622–2651, doi:10.1175/JCLI-D-11-00301.1.

Fita, L., J. Fernández, and M. Garcia-Dez, 2009: CLWRF: WRF modifications for regional climate simulation under future scenarios. *11th WRF Users Workshop,* Boulder, CO, NCAR. [Available online at http://www.meteo.unican.es/en/node/72915.]

Gent, P. R., and Coauthors, 2011: The Community Climate System Model version 4. *J. Climate,* **24,** 4973–4991, doi:10.1175/2011JCLI4083.1.

Giorgi, F., 2006: Regional climate modeling: Status and perspectives. *J. Phys. IV France,* **139,** 101–118, doi:10.1051/jp4:2006139008.

——, C. Jones, and G. R. Asrar, 2009: Addressing climate information needs at the regional level: The CORDEX framework. *WMO Bull.,* **58,** 175–183.

Grell, G. A., and D. Dévényi, 2002: A generalized approach to parameterizing convection combining ensemble and data assimilation techniques. *Geophys. Res. Lett.,* **29,** doi:10.1029/2002GL015311.

Gula, J., and W. R. Peltier, 2012: Dynamical downscaling over the Great Lakes Basin of North America using the WRF regional climate model: The impact of the Great Lakes system on regional greenhouse warming. *J. Climate,* **25,** 7723–7742, doi:10.1175/JCLI-D-11-00388.1.

Gutmann, E. D., R. M. Rasmussen, C. Liu, K. Ikeda, D. J. Gochis, M. P. Clark, J. Dudhia, and G. Thompson, 2012: A comparison of statistical and dynamical downscaling of winter precipitation over complex terrain. *J. Climate,* **25,** 262–281, doi:10.1175/2011JCLI4109.1.

Harris, I., P. D. Jones, T. J. Osborn, and D. H. Lister, 2014: Updated high-resolution grids of monthly climatic observations—The CRU TS3.10 dataset. *Int. J. Climatol.,* **34,** 623–642, doi:10.1002/joc.3711.

Hawkins, E., and R. Sutton, 2009: The potential to narrow uncertainty in regional climate predictions. *Bull. Amer. Meteor. Soc.,* **90,** 1095–1107, doi:10.1175/2009BAMS2607.1.

Holland, M. M., D. A. Bailey, B. P. Briegleb, B. Light, and E. Hunke, 2012: Improved sea ice shortwave radiation physics in CCSM4: The impact of melt ponds and aerosols on Arctic sea ice. *J. Climate,* **25,** 1413–1430, doi:10.1175/JCLI-D-11-00078.1.

Iacono, M. J., J. S. Delamere, E. J. Mlawer, M. W. Shephard, S. A. Clough, and W. D. Collins, 2008: Radiative forcing by long-lived greenhouse gases: Calculations with the AER radiative transfer models. *J. Geophys. Res.,* **113,** D13103, doi:10.1029/2008JD009944.

Jahn, A., and Coauthors, 2012: Late-twentieth-century simulation of Arctic sea ice and ocean properties in the CCSM4. *J. Climate,* **25,** 1431–1452, doi:10.1175/JCLI-D-11-00201.1.

Jin, J., and L. Wen, 2012: Evaluation of snowmelt simulation in the Weather Research and Forecasting model. *J. Geophys. Res.,* **117,** D10110, doi:10.1029/2011JD016980.

Kerkhoven, E., and T. Y. Gan, 2011: Differences and sensitivities in potential hydrologic impact of climate change to regional-scale Athabasca and Fraser River basins of the leeward and windward sides of the Canadian Rocky Mountains respectively. *Climatic Change,* **106,** 583–607, doi:10.1007/s10584-010-9958-7.

Knutti, R., and Coauthors, 2008: A review of uncertainties in global temperature projections over the twenty-first century. *J. Climate,* **21,** 2651–2663, doi:10.1175/2007JCLI2119.1.

Koster, R. D., and Coauthors, 2004: Regions of strong coupling between soil moisture and precipitation. *Science,* **305,** 1138–1140, doi:10.1126/science.1100217.

Lawrence, D. M., K. W. Oleson, M. G. Flanner, C. G. Fletcher, P. J. Lawrence, S. Levis, S. C. Swenson, and G. B. Bonan, 2012: The CCSM4 land simulation, 1850–2005: Assessment of surface climate and new capabilities. *J. Climate,* **25,** 2240–2260, doi:10.1175/JCLI-D-11-00103.1.

Luce, C. H., J. T. Abatzoglou, and Z. A. Holden, 2013: The missing mountain water: Slower westerlies decrease orographic enhancement in the Pacific Northwest USA. *Science,* **342,** 1360–1364, doi:10.1126/science.1242335.

Maraun, D., and Coauthors, 2010: Precipitation downscaling under climate change: Recent developments to bridge the gap between dynamical models and the end user. *Rev. Geophys.,* **48,** RG3003, doi:10.1029/2009RG000314.

Meehl, G. A., and Coauthors, 2012: Climate system response to external forcings and climate change projections in CCSM4. *J. Climate,* **25,** 3661–3683, doi:10.1175/JCLI-D-11-00240.1.

Mesinger, F., and Coauthors, 2006: North American Regional Reanalysis. *Bull. Amer. Meteor. Soc.,* **87,** 343–360, doi:10.1175/BAMS-87-3-343.

Miguez-Macho, G., G. L. Stenchikov, and A. Robock, 2004: Spectral nudging to eliminate the effects of domain position and geometry in regional climate model simulations. *J. Geophys. Res.,* **109,** D13104, doi:10.1029/2003JD004495.

Morrison, H., G. Thompson, and V. Tatarskii, 2009: Impact of cloud microphysics on the development of trailing stratiform precipitation in a simulated squall line: Comparison of one- and two-moment schemes. *Mon. Wea. Rev.,* **137,** 991–1007, doi:10.1175/2008MWR2556.1.

Mote, P. W., and E. P. Salathé, 2010: Future climate in the Pacific Northwest. *Climatic Change,* **102,** 29–50, doi:10.1007/s10584-010-9848-z.

Nakanishi, M., and H. Niino, 2009: Development of an improved turbulence closure model for the atmospheric boundary layer. *J. Meteor. Soc. Japan,* **87,** 895–912, doi:10.2151/jmsj.87.895.

Neale, R. B., J. Richter, S. Park, P. H. Lauritzen, S. J. Vavrus, P. J. Rasch, and M. Zhang, 2013: The mean climate of the Community Atmosphere Model (CAM4) in forced SST and fully coupled experiments. *J. Climate,* **26,** 5150–5168, doi:10.1175/JCLI-D-12-00236.1.

Phillips, A. S., C. Deser, and J. Fasullo, 2014: Evaluating modes of variability in climate models. *Eos, Trans. Amer. Geophys. Union,* **95,** 453, doi:10.1002/2014EO490002.

Pollock, E. W., and A. B. G. Bush, 2013: Changes in snow mass balance in the Canadian Rocky Mountains caused by CO_2 rise: Regional atmosphere model results. *Atmos.–Ocean,* **51,** 505–521, doi:10.1080/07055900.2013.852964.

Rasmussen, R., and Coauthors, 2011: High-resolution coupled climate runoff simulations of seasonal snowfall over Colorado: A process study of current and warmer climate. *J. Climate,* **24,** 3015–3048, doi:10.1175/2010JCLI3985.1.

Rayner, N. A., D. E. Parker, E. B. Horton, C. K. Folland, L. V. Alexander, D. P. Rowell, E. C. Kent, and A. Kaplan, 2003: Global analyses of sea surface temperature, sea ice, and night marine air temperature since the late nineteenth century. *J. Geophys. Res.,* **108,** 4407, doi:10.1029/2002JD002670.

Salathé, E. P., L. R. Leung, Y. Qian, and Y. Zhang, 2010: Regional climate model projections for the state of Washington. *Climatic Change,* **102,** 51–75, doi:10.1007/s10584-010-9849-y.

Schneider, U., A. Becker, P. Finger, A. Meyer-Christoffer, M. Ziese, and B. Rudolf, 2014: GPCC's new land surface precipitation climatology based on quality-controlled in situ data and its role in quantifying the global water cycle. *Theor. Appl. Climatol.,* **115,** 15–40, doi:10.1007/s00704-013-0860-x.

Seneviratne, S. I., T. Corti, E. L. Davin, M. Hirschi, E. B. Jaeger, I. Lehner, B. Orlowsky, and A. J. Teuling, 2010: Investigating soil moisture–climate interactions in a changing climate: A review. *Earth Sci. Rev.,* **99,** 125–161, doi:10.1016/j.earscirev.2010.02.004.

Shrestha, R. R., M. A. Schnorbus, A. T. Werner, and A. J. Berland, 2012: Modelling spatial and temporal variability of hydrologic impacts of climate change in the Fraser River basin, British Columbia, Canada. *Hydrol. Processes,* **26,** 1840–1860, doi:10.1002/hyp.9283.

Skamarock, W. C., and J. B. Klemp, 2008: A time-split nonhydrostatic atmospheric model for weather research and forecasting applications. *J. Comput. Phys.,* **227,** 3465–3485, doi:10.1016/j.jcp.2007.01.037.

——, and Coauthors, 2008: A description of the Advanced Research WRF version 3. NCAR Tech. Note NCAR/TN–475+STR, 113 pp.

Tewari, M., and Coauthors, 2004: Implementation and verification of the unified Noah land surface model in the WRF model. *20th Conf. on Weather Analysis and Forecasting/16th Conf. on Numerical Weather Prediction,* Seattle, WA, Amer. Meteor. Soc., 14.2a. [Available online at https://ams.confex.com/ams/84Annual/techprogram/paper_69061.htm.]

Trenberth, K. E., 1999: Atmospheric moisture recycling: Role of advection and local evaporation. *J. Climate,* **12,** 1368–1381, doi:10.1175/1520-0442(1999)012<1368:AMRROA>2.0.CO;2.

——, and J. W. Hurrell, 1994: Decadal atmosphere–ocean variations in the Pacific. *Climate Dyn.,* **9,** 303–319, doi:10.1007/BF00204745.

——, A. Dai, R. M. Rasmussen, and D. B. Parsons, 2003: The changing character of precipitation. *Bull. Amer. Meteor. Soc.,* **84,** 1205–1217, doi:10.1175/BAMS-84-9-1205.

——, L. Smith, T. Qian, A. Dai, and J. Fasullo, 2007: Estimates of the global water budget and its annual cycle using observational and model data. *J. Hydrometeor.,* **8,** 758–769, doi:10.1175/JHM600.1.

van der Ent, R. J., and H. H. G. Savenije, 2011: Length and time scales of atmospheric moisture recycling. *Atmos. Chem. Phys.,* **11,** 1853–1863, doi:10.5194/acp-11-1853-2011.

Wang, W., and Coauthors, 2012: ARW version 3 modeling system user's guide. NCAR Mesoscale and Microscale Meteorology Division, 384 pp. [Available online at http://www2.mmm.ucar.edu/wrf/users/docs/user_guide_V3.4/ARWUsersGuideV3.pdf.]